

THE FLORIDA STATE UNIVERSITY

COLLEGE OF ARTS AND SCIENCES

INTERANNUAL FLOW OFF SOUTHERN CALIFORNIA AND ITS
INFLUENCE ON WATER PROPERTIES AND MARINE LIFE.

By

MARCELO DOTTORI

A Dissertation submitted to the
Department of Oceanography
in partial fulfillment of the
requirements for the degree of
Doctor of Philosophy

Degree Awarded:
Spring Semester, 2007

The members of the Committee approve the Dissertation of Marcelo Dottori defended on November 20, 2006.

Allan J. Clarke
Professor Directing Dissertation

Christopher Tam
Outside Committee Member

Doron Nof
Committee Member

Georges Weatherly
Committee Member

Thorsten Dittmar
Committee Member

Approved:

William C. Burnett, Acting Chair
Department of Oceanography

Dean, College of Arts and Sciences

The Office of Graduate Studies has verified and approved the above named committee members.

This work is dedicated to Fabiana, who has been by my side during the hard moments encouraging me with a big smile.

ACKNOWLEDGEMENTS

I'd like to thank my committee members, Dr. Nof, Dr. Weatherly, Dr. Tam and Dr. Dittmar for their kindness in understanding my needs in the last few months. I specially thank Paula T. Jahromi and Steve VanGorder for all the support during these 5 years at FSU.

I deeply thank my advisor, Dr. Allan J. Clarke, for all the support, patience and great ideas since I arrived in Tallahassee, in January 2002. I am really glad to have worked with him during the past 5 years, not only for his knowledge in the field, but also for the great person he has shown to be, very much above my expectations.

Finally, I also acknowledge the financial support of the Brazilian National Council for the Development of Science and Technology (CNPq-200132/2001-6) and NSF grant OCE-0220563, which made this thesis possible.

TABLE OF CONTENTS

List of Tables	vi
List of Figures	vii
Abstract	x
1. INTRODUCTION	1
2. TOO FAST PLANETARY WAVE PROPAGATION OFF CALIFORNIA AND ITS EFFECT ON ZOOPLANKTON	5
2.1 Introduction	5
2.2 Westward propagation of dynamic height in the gappy 1949-2001 CalCOFI record	7
2.3 Westward propagation of sea level height as measured by satellites	10
2.4 Theoretical wave speeds	12
2.5 Interannual fluctuations in the California Current	14
2.6 Interannual fluctuations in California Current zooplankton	17
2.7 Concluding remarks	21
3. ROSSBY WAVE, EVAPORATION AND THE INTERANNUAL AND DECADEAL VARIABILITY OF SALINITY AND TEMPERATURE OFF CALIFORNIA	23
3.1 Introduction	23
3.2 Westward propagating low-frequency waves and their currents	24
3.3 Estimation of the vertical function $F(z)$	26
3.4 Salinity anomalies	35
3.5 Observed and model salinity anomalies	39
3.6 Concluding remarks	43
4. CONCLUSIONS	48
APPENDIX	50
A. The effect of mean meridional flow on long Rossby waves	50
REFERENCES	53
BIOGRAPHICAL SKETCH	55

LIST OF TABLES

- 1.1 Correlation and regression coefficients between time series of interannual sea-level at San Diego and other tide-gauge stations at the coast of California. The filtering process is the same as was used for Fig. 1.2 and it was applied to all the time-series. The maximum correlation is obtained for zero lag. 4

- 3.1 For each of the 6 regions, the depth of maximum (in magnitude) correlation between observed S' and η' , the value of the correlation coefficient, the corresponding observed regression coefficient with error bars and the regression coefficient expected from theory (see (3.31)). 40

LIST OF FIGURES

1.1	Schematic of the dynamics in the central equatorial Pacific for low-frequency variability.	2
1.2	Interannual sea-level at San Diego and NIÑO3.4. The monthly time-series of sea-level was filtered by, first, removing the trend and, then, removing the monthly means for each of the 12 calendar months. After that, a filter based on Trenberth[1] was applied. This filter is a symmetric 11-point low-pass filter that passes more than 80% of the amplitude at periods of 24 months and longer and passes less than 10% of the amplitude for periods shorter than 8 months. The correlation between the 2 time series is maximum for zero lag with a correlation coefficient of 0.70.	3
2.1	The CalCOFI region off Southern California showing the satellite tracks and 63 frequently sampled CalCOFI stations. The stations are grouped into 6 sets according to their zonal distance from the coast in bins of approximately 130 km. Specifically, the solid inverted triangles represent all stations within 130 km of the coast, shaded circles all stations between 130 km and 260 km from the coast, solid hexagons stations 260 km - 390 km from the coast, etc. . . .	8
2.2	Gappy time series of anomalous dynamic height averaged over each of the 6 groups of stations in Fig. 1.2. (a) The shaded-diamond group; (b) the solid-triangle group; (c) the shaded-square group; (d) the solid-hexagon group; (e) the shaded-circle group; and (f) the solid-inverted triangle group. Panel (g) is the complete monthly record of anomalous San Diego sea level. The solid line in panel (g) representing the interannual sea level was found using the low-pass Trenberth (1984) interannual filter (see 2.2).	9
2.3	Estimates of westward Rossby wave propagation speed off California using CalCOFI hydrographic data (solid regression line, solid diamond), TOPEX / Jason1 sea level heights (dotted regression line, solid circles), standard first baroclinic mode long Rossby wave theory (dash-dot regression line, open triangles), long Rossby wave theory with the large scale California current included (dashed regression line, open squares) and long Rossby wave theory with both the large scale California current and varying bottom topography included (Killworth and Blundell theory, solid line, star data points).	11

2.4	Regression coefficients for each of the lagged CalCOFI dynamic height time series on the Trenberth (1984) filtered San Diego time series (inverted solid triangles) and the corresponding results for the satellite time series. The dynamic height and satellite time series were appropriately lagged to remove phase differences with San Diego sea level due to wave propagation; in this way the change in amplitude of the propagating signal could be estimated.	12
2.5	Normal and tangential coordinates (n,s) to a coastline making an angle θ with due north.	18
2.6	Monthly anomalies of the logarithm of zooplankton volume concentration averaged over the CalCOFI region plotted against anomalies of the dynamic height averaged over the CalCOFI region. The correlation coefficient is 0.64 and the regression coefficient, 0.9 with an error of 0.3 at a confidence level of 90%.	19
2.7	Lagged correlation of interannual $\ln n$ averaged over the CalCOFI region with monthly anomalous negative San Diego sea level (η'). A positive lag means η leads $\ln n$	21
3.1	Correlation coefficients between anomalies of temperature and anomalies of dynamic height. The solid square represents the maximum correlation in the first 500 meters. The regions are separated according to Fig. 2.1.	28
3.2	Regression coefficients between anomalies of temperature and anomalies of dynamic height. The solid square represents the maximum correlation in the first 500 meters. The regions are separated according to Fig. 2.1.	29
3.3	Temporally averaged temperature for the whole CalCOFI record at the 6 binned CalCOFI regions (see Fig. 2.1). The isotherm slopes are generally positive toward the north.	30
3.4	Temporally averaged density for the whole CalCOFI record at the 6 binned CalCOFI regions (see Fig. 2.1). The pycnocline slopes are generally positive toward the north.	31
3.5	Temporally averaged N^2 for the whole CalCOFI record at the 6 binned CalCOFI regions (see Fig. 2.1).	32
3.6	Vertical empirical modes $F(z)$ obtained from equation (3.17) and the regression coefficients shown in Fig. 3.2. The empirical modes are only calculated from the surface up to 200 meters deep, where the correlation is relatively high, assuming that the vertical modes are unity at the surface.	33
3.7	Average (a) salinity, (b) temperature and (c) Brunt-Vaisala frequency for the CalCOFI region using NODC-World Ocean Atlas Data (website address http://www.cdc.noaa.gov/cdc/data.nodc.woa98.html). The first vertical mode profile (d) calculated using the data in (c).	34

3.8	Temporally averaged salinity for the whole CalCOFI record at the 6 binned CalCOFI regions (see Fig. 2.1). The isohaline slopes are generally negative toward the north.	38
3.9	Correlation coefficients between anomalies of salinity and anomalies of dynamic height. The solid square represents the maximum correlation in the first 500 meters. The regions are grouped according to Fig. 2.1.	41
3.10	Regression coefficients between anomalies of salinity and anomalies of dynamic height. The solid square represents the maximum correlation in the first 500 meters. The regions are separated according to Fig. 2.1.	42
3.11	Interannual coastal La Jolla surface salinity anomaly (solid curve), 5 meter depth coastal La Jolla salinity anomaly (dashed curve) and the anomalous salinity averaged over region 1 in the upper 100 meters of the water column (dots). The correlation between each coastal time series and region 1 is 0.86 which is significantly different from zero (critical regression at 95%=0.59) according to Ebisuzaki (1997)[2]. The coastal surface and 5 m depth salinity time series were obtained from the Stephen Birch Aquarium-Museum at the Scripps Institute of Oceanography.	44
3.12	Observed region 1 CalCOFI salinity anomalies averaged over the upper 100 meters of the water column (large dots), coastal La Jolla surface (small dots), 5 m depth (dash-dot) and predicted anomalous salinity (solid line). The correlation coefficients are significantly different from zero at the 90% level for region 1 CalCOFI time series and 95% for La Jolla salinity at the surface and 5 meters deep according to Ebisuzaki (1997) [2].	45
3.13	Advective (solid line) and evaporative (dashed line) contributions to anomalous salinity according to (3.38). In Eq. (3.38) the advective contribution is proportional to η' and the evaporative contribution is proportion to the time integral of E'	46
3.14	(a) Wind speed $ \mathbf{u}_a $, (b) specific humidity different $q_s - q_a$ and (c) anomalous evaporation E' over the CalCOFI region using the International Comprehensive Ocean Atmosphere Data Set (ICOADS) (http://icoads.noaa.gov/).	47

ABSTRACT

Lagged correlation of dynamic height from the gappy California Cooperative Oceanic Fisheries Investigation (CalCOFI) with monthly San Diego sea level for the period 1949-2001 shows that the dynamic height propagates westward at 4.10 cm/s, about double the speed of the large-scale low frequency Rossby wave (2.2 cm/s). TOPEX/Poseidon/Jason1 along-track sea level height estimates since January 1993, filtered interannually, propagate westward at 4.3 cm/s, verifying that observed westward propagation is about double that expected. Including the effect of the mean California current on the Rossby wave propagation does not explain the discrepancy but rather slightly increases it. If variations in the ocean depth in the CalCOFI region are also taken into account, the westward propagation is still only about one half that observed. Standard theory therefore does not explain the observations.

Because of the westward propagation, interannual variations in alongshore geostrophic surface current are proportional to the time derivative of sea level. This means that such large scale interannual current variability can be monitored with appropriate lag, by the time derivative of coastal sea level. The anomalous alongshore flow advects particles, the anomalous alongshore particle displacement being proportional to sea level. Since nutrient concentration is lower in the south, the anomalous alongshore displacement results in lower nutrient concentration when sea level is anomalously high and higher nutrient concentration when the sea level is anomalously low. Vertical displacement also results in a similar relationship between nutrients and sea level, so it is not surprising that sea level anomalies are strongly related to fluctuations in zooplankton population. In fact, consistent with the westward Rossby wave propagation, the logarithm of the zooplankton population averaged over the CalCOFI region is well correlated with coastal sea level anomalies and lags it by

about 2 months. By this result monthly anomalous San Diego sea level can be used to monitor and predict interannual changes in the zooplankton population.

The anomalous alongshore and vertical particle displacements associated with the Rossby waves also act on the mean temperature and salinity fields to produce temperature and salinity anomalies. Theory suggests that these anomalies should be proportional to the anomalous dynamic height. Consistent with this, observed salinity anomalies at depths of 100-200 m are well correlated with dynamic height anomalies. At depths greater than 200 m the observed anomalies are small and, consistent with a smaller signal to noise ratio, the correlation falls. At depths shallower than 100 m the correlation between salinity and dynamic height anomalies also falls rapidly. This is at least partly because of anomalous evaporation which drives an interdecadal surface ocean salinity response. The flow anomalies can similarly be used to explain the temperature fluctuations except that the correlation between temperature and dynamic height fluctuations does not fall rapidly in the surface layer as in the salinity case, suggesting that in the surface layer anomalous advection rather than surface heat flux is mainly responsible for the surface layer temperature anomalies.

CHAPTER 1

INTRODUCTION

When an El Niño occurs, the winds in the coastal equatorial Pacific are anomalously westerly and push the surface layer water above the thermocline eastward, making the sea-level anomalously high (see Fig. 1.1) and the thermocline anomalously deep in the eastern equatorial Pacific and at the South American coast. The deepened thermocline also results in an increased sea surface temperature and fewer nutrients near the ocean surface where there is light. Fewer nutrients in the well-lit surface ocean layer cause a decline in phytoplankton and, as a result, a dramatic decrease in the population of fish and mammals.

Although El Niño is an event that occurs in the equatorial region off the western coast of South-America, its impact can be observed at coastal regions very far from the equator, such as the western coasts of the United States and Chile. One of the first works to observe El Niño events associated with sea-level variances in a very broad range of latitudes was by Enfield and Allen [3]. They observed a coherent variability of well known El Niño events with the sea-level variability from Antogogasta, Chile, ($23^{\circ}S$) to San Francisco, California ($38^{\circ}N$). Chelton and Davis [4] also observed an interannual signal that propagates poleward from the equator and, since then, beginning with Chelton et al (1982)[5], several authors have analyzed El Niño events associated with coastal variability of water properties and marine life. Although associations between El Niño/La Niña cycles, coastal water properties and marine life away from the equator are relatively well documented, the understanding of the dynamics itself is not well known.

At the coast of California, specifically, El Niño/La Niña cycles are strongly correlated with the sea-level variability. Figure 1.2 shows the similarity of the interannual variability of sea-level at San Diego and NIÑO3.4, a climate index that estimates the anomalous warming at the equatorial eastern Pacific. Also, the interannual sea-level at San Diego and the

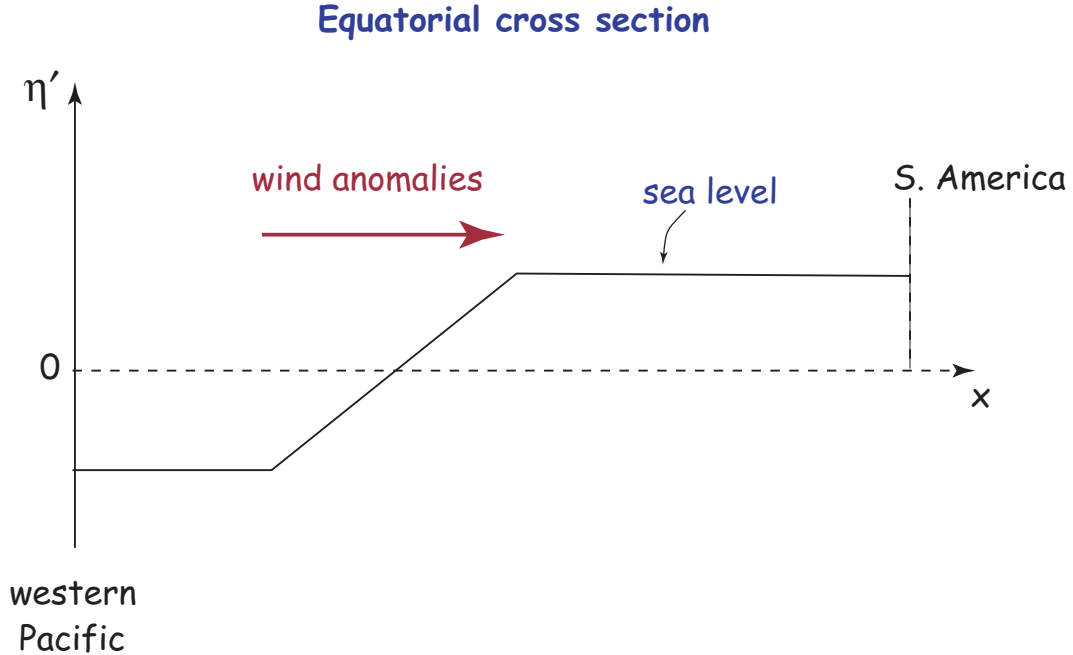


Figure 1.1: Schematic of the dynamics in the central equatorial Pacific for low-frequency variability.

interannual sea-level at several tide-gauge stations along the coast of California are highly correlated with regression coefficients close to 1 (Table 1.1). This suggests that the whole coast of California is impacted by El Niño events and the interannual dynamics must be, somehow, connected to this equatorial remote forcing.

The purpose of this dissertation is to better understand the interannual dynamics at the California coast and its effects on temperature, salinity and zooplankton population. In order to achieve that, the main data sets used here are vertical profiles of temperature, salinity and zooplankton volume, provided by the California Cooperative Oceanic Fishery Investigations (CalCOFI), and satellite altimeter data from TOPEX/Jason1. Other data sets are also used, but not as extensively as the ones just mentioned.

The next chapter shows how the interannual sea-level at the coast propagates offshore as Rossby waves, with a consistent estimate of the propagation speed by both dynamic height and satellite altimeter estimated sea level. It also shows how the zooplankton population is affected by this dynamics. In chapter 3, the interannual temperature and low-frequency

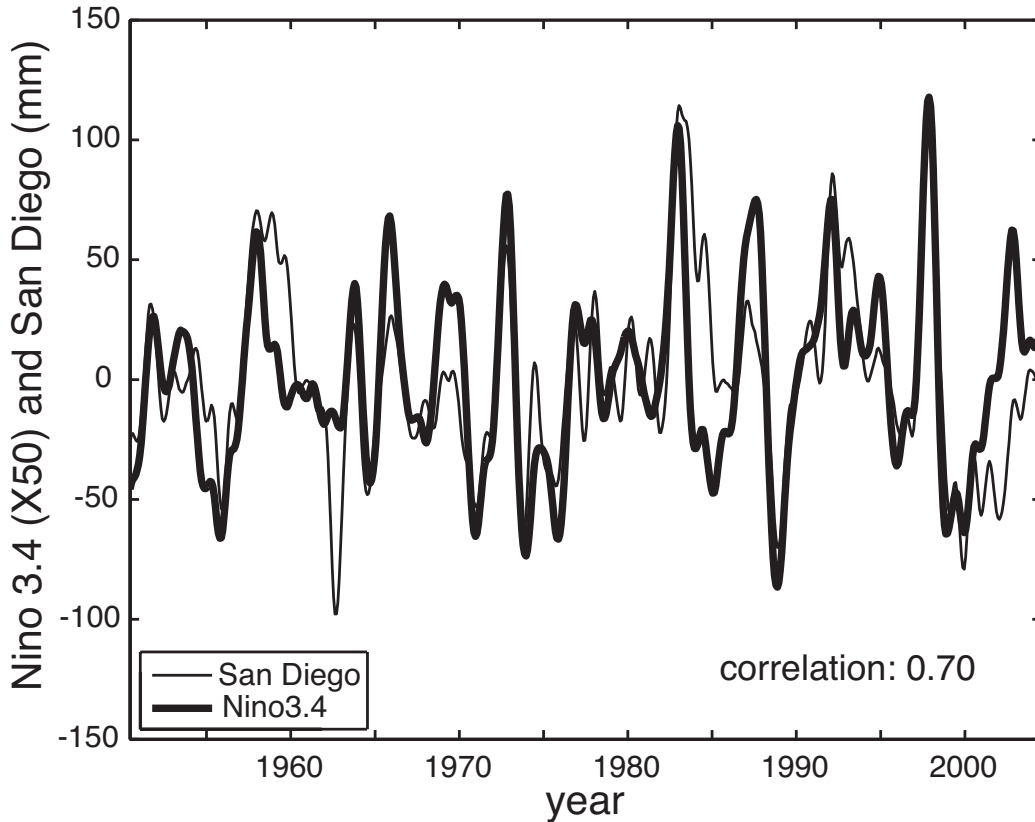


Figure 1.2: Interannual sea-level at San Diego and NIÑO3.4. The monthly time-series of sea-level was filtered by, first, removing the trend and, then, removing the monthly means for each of the 12 calendar months. After that, a filter based on Trenberth[1] was applied. This filter is a symmetric 11-point low-pass filter that passes more than 80% of the amplitude at periods of 24 months and longer and passes less than 10% of the amplitude for periods shorter than 8 months. The correlation between the 2 time series is maximum for zero lag with a correlation coefficient of 0.70.

salinity are analyzed based on this Rossby wave dynamics. Chapter 3 also shows that salinity has a strong interdecadal signal, due to evaporation, that is not associated with the remote equatorial interannual signal. Finally, Chapter 4 summarizes the main results of this thesis.

Table 1.1: Correlation and regression coefficients between time series of interannual sea-level at San Diego and other tide-gauge stations at the coast of California. The filtering process is the same as was used for Fig. 1.2 and it was applied to all the time-series. The maximum correlation is obtained for zero lag.

location	latitude	correlation	regression
Los Angeles	$33^{\circ}N$	0.9	0.85
Monterey	$35^{\circ}N$	0.95	0.97
San Francisco	$36^{\circ}N$	0.78	0.92
Crescent City	$38^{\circ}N$	0.81	1.0

CHAPTER 2

TOO FAST PLANETARY WAVE PROPAGATION OFF CALIFORNIA AND ITS EFFECT ON ZOOPLANKTON

2.1 Introduction

Consistent with the discussion in chapter 1, analysis of sea level, sea surface temperature (SST) and thermocline observations (Enfield and Allen 1980[3]; Chelton and Davis 1982[4]; Kessler 1990[6]) have shown that much of the interannual variability along the California coast originates along the equator; California sea level and SST tend to be higher than normal and the thermocline depth greater during El Niño while during La Niña sea level and SST tend to be lower than normal and the thermocline shoals. Based on low-frequency theory (see, e.g., Schopf et al. 1981[7]; Cane and Moore 1981[8]; Clarke 1983[9]) the interannual sea level signal seen along the coast of California should propagate westward as long Rossby waves. White and Saur (1983)[10] and Kessler (1990)[6] both provided bathythermographic evidence for such long interannual waves leaving the coast south of $30^{\circ}N$ but so far there has been no documentation of long interannual Rossby waves propagating westward from the coast north of $30^{\circ}N$. In fact, in their analysis of bathythermographic data along the great circle route between San Francisco and Hawaii, White and Saur (1983)[10] found no evidence of waves propagating westward from the coast north of $30^{\circ}N$ for reasons unknown. Miller et al.(1997)[11], based on a coarse resolution 5° longitude by 2° latitude grid, concluded that north of $25^{\circ}N$ interannual ocean variability in the interior ocean is due to interannual wind stress curl forcing rather than the boundary signal propagating westward from the coast.

In section 2.2 a search is made for Rossby waves in the data-rich region off California where hydrographic and other oceanographic measurements have been made since 1949 under the California Cooperative Oceanic Fisheries Investigation (CalCOFI). It's found

that dynamic height does propagate westward at a speed independently checked in section 2.3 using the shorter decade-long satellite sea level estimates. Although both propagation estimates agree very well, the speed is double that expected.

Past theoretical studies (Killworth et al. 1997[12]; Dewar 1998[13]; Dewar and Morris 2000[14]) have suggested that Rossby waves may propagate faster due to the influence of large-scale zonal ocean currents. But in section 2.4, when the theory of Killworth et al. (1997)[12] is used to calculate wave propagation speeds with the zonal component of the mean California current included, it is found that the discrepancy between theory and observation is even larger! Mean meridional coastal flow can also strongly affect low-frequency coastal ocean dynamics (Clarke and Li 2004[15]), but the theory developed in Appendix A shows that while the California meridional mean flow component affects the Rossby wave amplitude, it has no effect on the wave speed. Slowly varying changes in ocean depth can also affect the propagation speed (Killworth and Blundell 2002[16]), but in section 2.4 it is shown that even when both topographic variations and mean California current flow are included, the speed of the westward propagating interannual signal is still only about half that observed.

An awareness of the westward wave propagation is needed to understand interannual variations in the California current. Schneider et al. (2005)[17] showed that the flow anomalies are independent of large-scale climate indices. They suggested that the flow anomalies might be due to unresolved, small-scale atmospheric forcing or intrinsic ocean mesoscale variations prevalent in the California current. Based on the Schneider et al. result that the flow anomalies are independent of large scale climate indices, it might be expected that the San Diego sea level, which is well correlated with the El Niño index NINO3.4 (see Fig. 1.2), should also be uncorrelated with the flow anomalies. In section 2.5 it is shown that, based on the observed westward wave propagation, the coastal flow anomalies are indeed uncorrelated with interannual San Diego sea level. However, the coastal flow anomalies are still directly related to the large-scale dynamics since they are proportional to the time derivative of interannual San Diego sea level. In fact, the large scale interannual variations in the California current can be estimated and predicted using the time derivative of San Diego sea level.

Chelton et al. (1982)[5] and Roesler and Chelton (1987)[18] examined the close connection between interannual California current variability and fluctuations in zooplankton. In section 2.6 it is shown how interannual California currents and Rossby wave dynamics explain

why monthly coastal sea level anomalies can be used to monitor and predict interannual fluctuations in the California current zooplankton population.

2.2 Westward propagation of dynamic height in the gappy 1949-2001 CalCOFI record

The collapse of the sardine population off California spurred the formation of CalCOFI. Since 1949 CalCOFI cruises have gathered physical, chemical and biological data from the California current system (official website: <http://www.calcofi.org>). Probably no other large region in the world has been so intensely sampled for so many years. Even so, the data set has its shortcomings as the intensity of the sampling and the region covered have varied considerably. We will concentrate on 63 frequently sampled stations between San Diego and Monterey for the period 1949-2001 (see Fig. 2.1).

In order to check whether sea level propagates westward at low frequencies, ideally monthly dynamic height should be available at each station. Such height, based on a level of no motion at 500 m depth, can be calculated from salinity and temperature profiles when both are available for a given month. On those occasions when profiles were taken, usually both salinity and temperature were recorded. However, there were a small number of cases when salinity was missing. In these cases we used the average T-S relationship for that location and calendar month to determine the salinity. Small gaps in the vertical temperature profile of two points or less were linearly interpolated. In rare cases when there were gaps bigger than 2 consecutive points the profile was abandoned.

Based on their zonal distance from the coast, the dynamic height data were grouped (see Fig. 2.1) to form 6 separate, gappy monthly time series. Dynamic height anomalies were then formed by subtracting out the mean and the seasonal cycle. For example, the anomaly for (say) January 1998 is defined as the January 1998 value minus the average of all the January values available. The resultant gappy anomaly time series are shown in Fig. 2.2.

Lagged correlations of each of the six gappy time series with the complete monthly sea level anomaly time series at San Diego filtered with a Trenberth (1984)[1] interannual filter were then calculated. Low-pass Trenberth filter passes more than 80% of the amplitude at a period of 24 months and longer and less than 10% of the amplitude for periods shorter than 8 months. We recorded the lag for each time series when the correlation is maximum. The

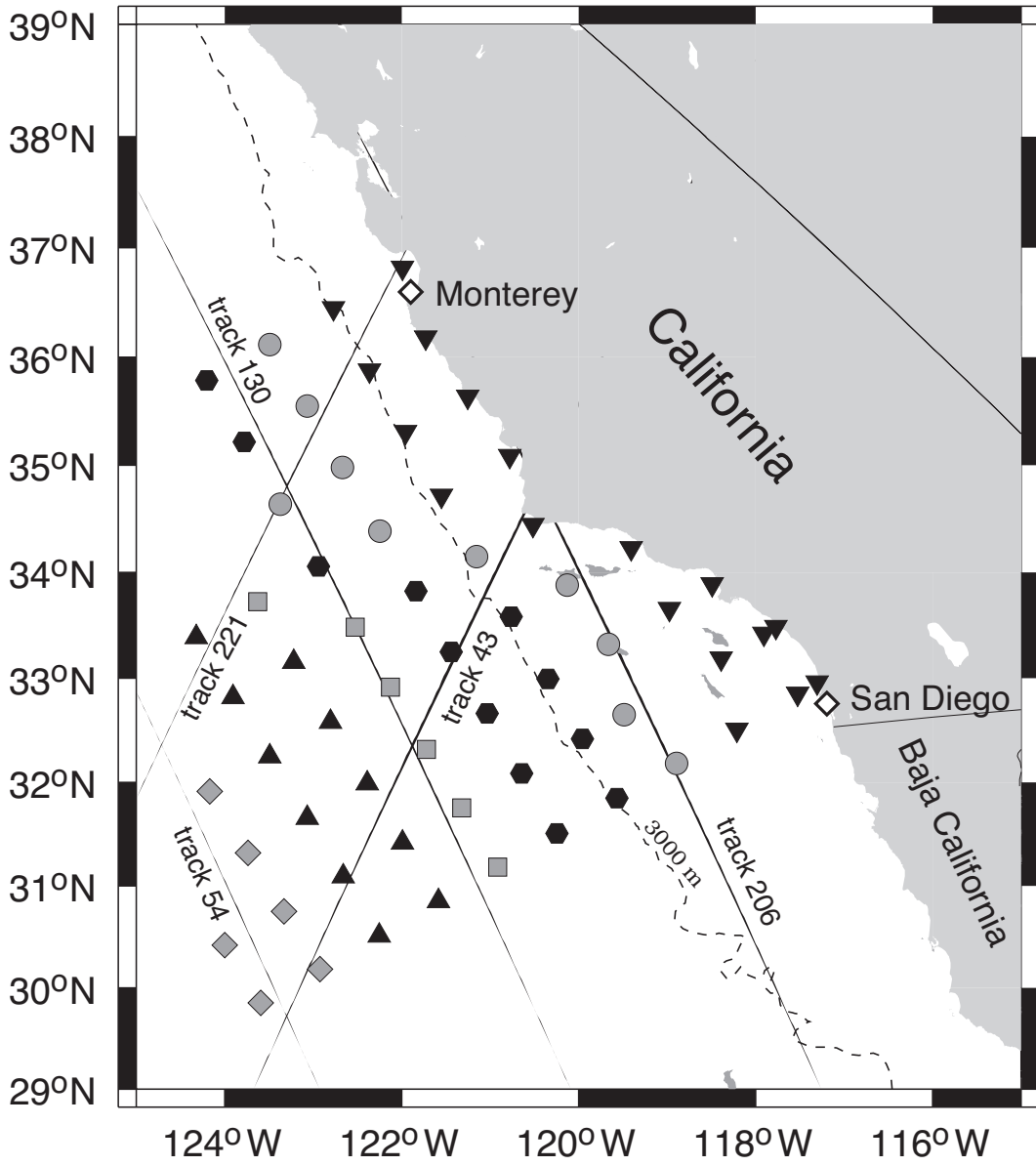


Figure 2.1: The CalCOFI region off Southern California showing the satellite tracks and 63 frequently sampled CalCOFI stations. The stations are grouped into 6 sets according to their zonal distance from the coast in bins of approximately 130 km. Specifically, the solid inverted triangles represent all stations within 130 km of the coast, shaded circles all stations between 130 km and 260 km from the coast, solid hexagons stations 260 km - 390 km from the coast, etc.

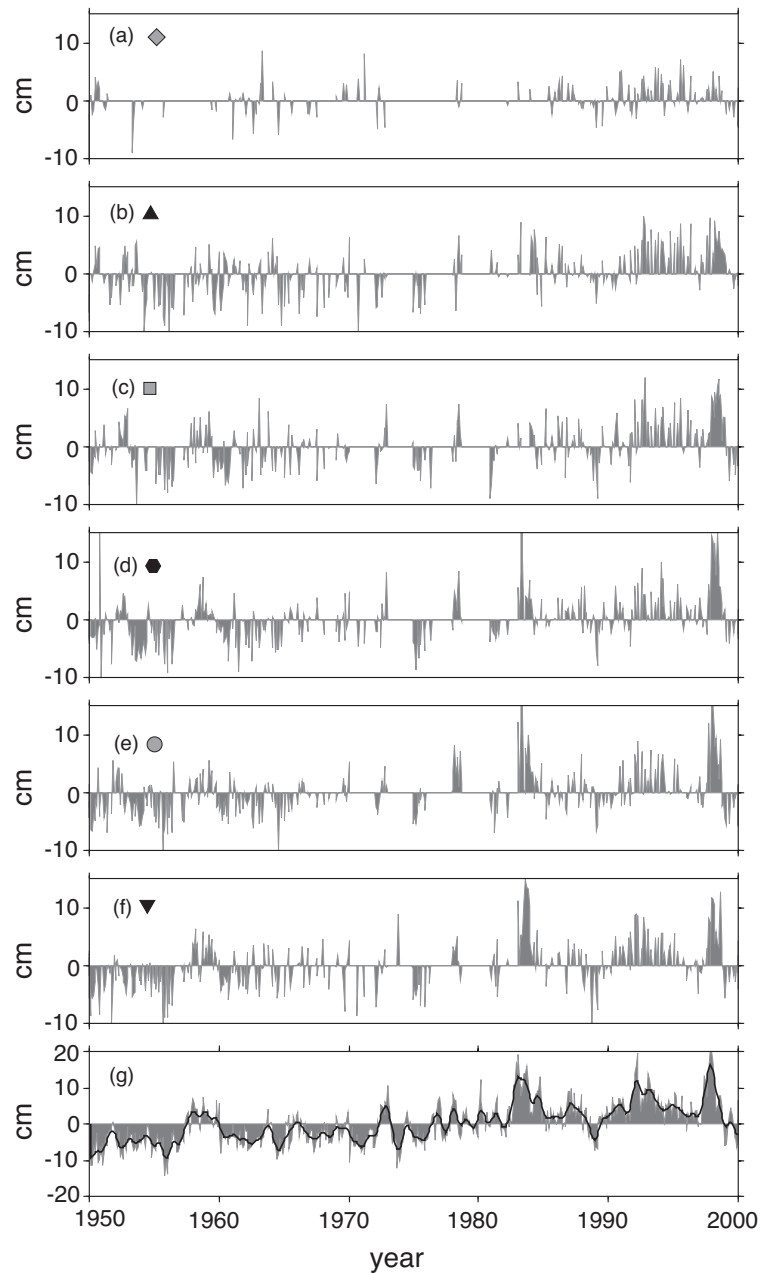


Figure 2.2: Gappy time series of anomalous dynamic height averaged over each of the 6 groups of stations in Fig. 1.2. (a) The shaded-diamond group; (b) the solid-triangle group; (c) the shaded-square group; (d) the solid-hexagon group; (e) the shaded-circle group; and (f) the solid-inverted triangle group. Panel (g) is the complete monthly record of anomalous San Diego sea level. The solid line in panel (g) representing the interannual sea level was found using the low-pass Trenberth (1984) interannual filter (see 2.2).

number of terms in each correlation was equal to the number of dynamic height estimates available in each gappy dynamic height time series since the San Diego time series had no gaps. Figure 2.3 shows the lags (solid diamonds) and the corresponding regression line between lag and zonal distance from the coast. The regression line (solid line) corresponds to a westward propagation of 4.10 cm/s. The speed of the first vertical mode long Rossby wave speed varies latitudinally like the reciprocal of the Coriolis parameter squared but calculations show that it is always within 20% of 2.0 cm/s in the CalCOFI region. This is about half of the observed 4.10 cm/s westward propagation. More detailed calculations in 2.4, estimating the meridionally-averaged theoretical Rossby wave speed from the same measurement points used in observations, give a Rossby wave speed of 2.18 cm/s (see 2.4).

Figure 2.4 suggests that the westward propagating signal decreases in amplitude with distance from the coast. The decrease is slight over the CalCOFI region if we ignore the last CalCOFI point which is based on fewer data than the other points. The falling amplitude is consistent with the results of White and Saur (1983)[10], who did not observe Rossby waves reaching the San Francisco/Hawaii ship track, and also with the coarse resolution results of Miller et al. (1997)[11] and the satellite sea level height results of Fu and Qiu (2002)[19]. The amplitude fall is not explained by the effect of the mean meridional flow of the California current on the interannual signal since theory (Appendix A) predicts an amplitude increase of about 50% over the measurement array.

2.3 Westward propagation of sea level height as measured by satellites

Along-track TOPEX/Poseidon/Jason1 satellite-estimated sea level height data available through the website (<http://podaac-www.jpl.nasa.gov/>) are analyzed. The data cover the period January 1993-December 2001 and the region $29^{\circ}N$ - $39^{\circ}N$, $124^{\circ}W$ - $116^{\circ}W$ (see Fig. 2.1). The data coverage shown in the figure is not continuous due to satellite data inaccuracies near the coast or islands. From each along-track measurement location individual 10-day measurements were combined to form monthly sea level time series. As for dynamic height, monthly sea level height anomalies were calculated for the same six regions as in the CalCOFI dynamic height analysis in the previous section. In the satellite case the monthly record is a lot shorter but complete in time so both the satellite time series and the San

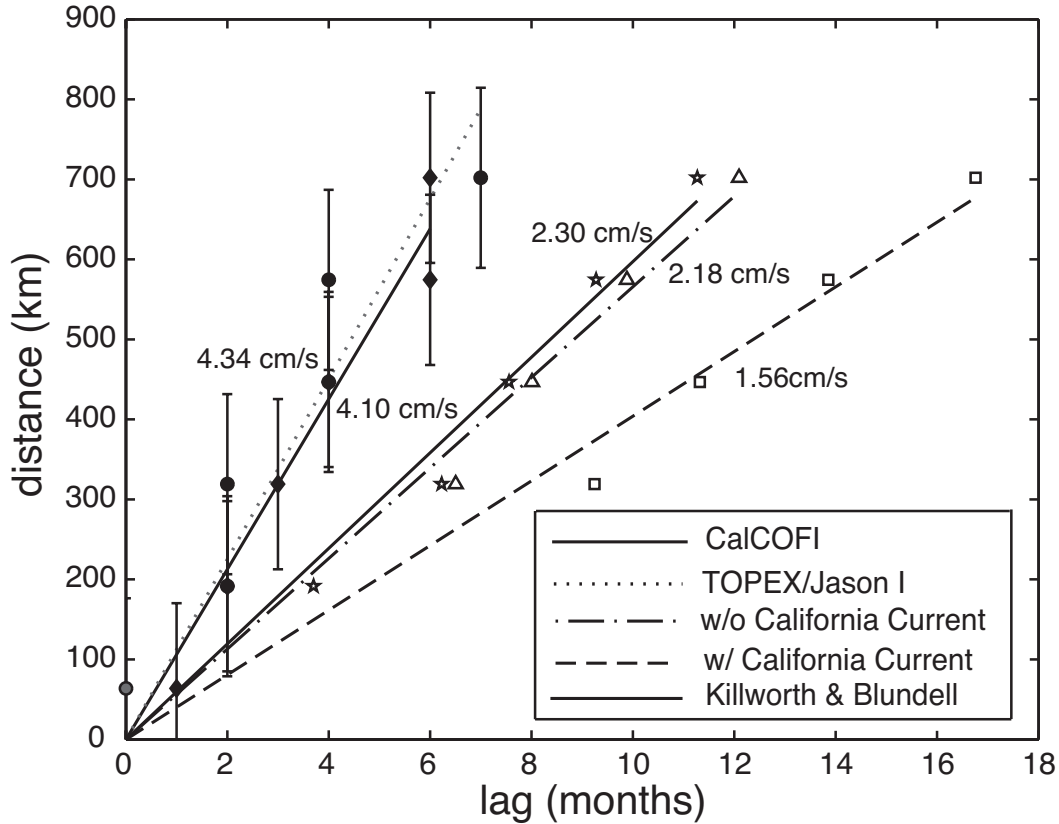


Figure 2.3: Estimates of westward Rossby wave propagation speed off California using CalCOFI hydrographic data (solid regression line, solid diamond), TOPEX / Jason1 sea level heights (dotted regression line, solid circles), standard first baroclinic mode long Rossby wave theory (dash-dot regression line, open triangles), long Rossby wave theory with the large scale California current included (dashed regression line, open squares) and long Rossby wave theory with both the large scale California current and varying bottom topography included (Killworth and Blundell theory, solid line, star data points).

Diego sea level time series could be filtered with the interannual filter used by Trenberth (1984)[1].

Lag correlations between the satellite and San Diego time series gave a westward propagation speed (4.34 cm/s) similar to that obtained using dynamic height (see Fig. 2.3). As for the dynamic height, regression coefficients corresponding to the correlations show a fall in the amplitude of the signal with distance from the coast (see Fig. 2.4).

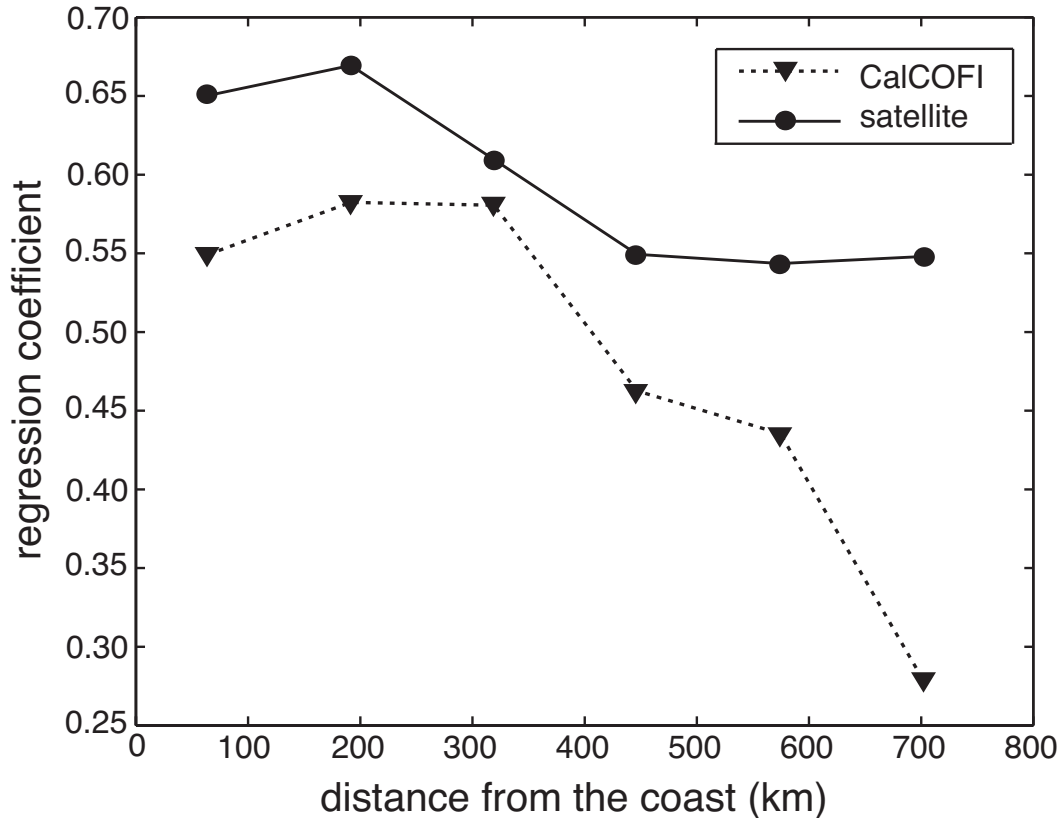


Figure 2.4: Regression coefficients for each of the lagged CalCOFI dynamic height time series on the Trenberth (1984) filtered San Diego time series (inverted solid triangles) and the corresponding results for the satellite time series. The dynamic height and satellite time series were appropriately lagged to remove phase differences with San Diego sea level due to wave propagation; in this way the change in amplitude of the propagating signal could be estimated.

2.4 Theoretical wave speeds

The close agreement between CalCOFI and satellite wave speed estimates indicates that long waves propagate westward from the California coast at a speed of about 4 cm/s. As noted earlier in section 2.2 (see also the dash-dot line in Fig. 2.3), this speed is about twice the standard first baroclinic long Rossby wave speed. The mean flow in the region may have an influence, so the westward speed was calculated using the theory of Killworth et al(1997)[12]. This linear theory assumes that the stratified ocean is of constant depth H and allows for a large-scale zonal mean flow. The westward propagation speed c satisfies the

following eigenvalue problem for unforced flow:

$$(\bar{u} - c) W_{zz} - u_z W_z + \frac{\beta N^2}{f^2} W = 0 \quad (2.1)$$

$$W = 0 \quad \text{at } z = 0, -H \quad (2.2)$$

In (2.1) and (2.2) $W(z)$ is the vertical velocity eigenfunction, N the buoyancy frequency, f the Coriolis parameter and β its northward gradient. When $\bar{u} \equiv 0$, the above problem reduces to standard linear normal mode theory (see, e.g., Gill 1982[20]). When $\bar{u} \neq 0$, (2.1) and (2.2) reduce to the matrix equation

$$AW = cBW, \quad (2.3)$$

where A and B are tri-diagonal matrices.

To solve (2.3), \bar{u} and N must be estimated. These functions were obtained on a grid using Levitus hydrographic data (Levitus 1982[21]) and, for \bar{u} , a level of no motion at 500 m. Calculations were done only in water at least 3000 m deep where the water depth was approximately constant. Solutions for the fastest vertical mode varied from 1 cm/s in the northern part of the CalCOFI region to 4 cm/s in the south.

To compare the theoretical results with the observations, theoretical lags were calculated at the same grid points as the observations using the theoretical speeds and known zonal distance from the coast. In theory this map of lags can be divided into the same six regions that were used for the CalCOFI and satellite data. However, the two regions closest to the coast only contain points in the north since the southern region is shallower than 3 km. Since the speeds are much slower in the north, we decided not to bias our calculations by including the two regions closest to the coast.

Figure 2.3 shows the theoretical wave speed estimates based on four of the six regions and zero lag at the coast. As noted earlier, when $\bar{u} = 0$, the westward propagation speed is 2.18 cm/s, only about one half of that observed. Inclusion of the large-scale zonal California current flow gives a westward speed of 1.56 cm/s, differing even more from the observations.

Clarke and Li (2004)[15] showed that meridional flow can strongly affect coastal inter-annual variability. In Appendix A we develop theory for the effect of meridional flow on

westward propagating Rossby waves. However, the theory does not predict a change in the westward propagation speed.

Killworth and Blundell (1999)[22] examined how slowly varying water depth affects the wave speed. However, even when both varying bottom topography and zonal mean flow are included in the theory (Killworth and Blundell 2002[16]), CalCOFI wave speeds are still only about half the observed speeds (Fig. 2.3).

Tailleux and McWilliams (2001)[23] have suggested that if the deep ocean can somehow be decoupled from the upper ocean, then the baroclinic wave propagation speed will be increased. However, it is not clear whether such decoupling occurs in the CalCOFI region. Furthermore, the decoupled wave propagation speed is less than that observed.

It seems that no standard theory can explain the observed propagation. This issue will not be pursued further here. Instead, the observed westward propagation will be analyzed to understand interannual fluctuations in the California current (2.5) and zooplankton (2.6).

2.5 Interannual fluctuations in the California Current

Chelton et al. (1982)[5] used an EOF analysis to describe interannual variability in the California current and showed that such variability is correlated with coastal interannual sea level and El Niño. On the other hand, Schneider et al. (2005)[17] showed that the flow anomalies are independent of large scale climate indices. These conclusions seem contradictory.

In order to understand the above conclusions using the observed westward propagation results from section 2.2, first note that the sea level and dynamic height anomalies satisfy

$$-\eta'_t + \gamma\eta'_x = 0, \tag{2.4}$$

where $\gamma \approx 4.2\text{cm/s}$. By geostrophy and (2.4), the north-south component of the fluctuating surface interannual flow is

$$\frac{g}{f} \frac{\partial \eta'}{\partial x} = \frac{g}{f\gamma} \frac{\partial \eta'}{\partial t}. \tag{2.5}$$

However, (2.5) does not describe the alongshore interannual fluctuations in the California current since these fluctuations are not north-south. Instead, we must estimate

$$v' = \frac{g}{f} \frac{\partial \eta'}{\partial n} = \frac{g}{f} \mathbf{e}_n \cdot \nabla \eta', \quad (2.6)$$

where n is the distance normal to the coast (see Fig. 2.5), \mathbf{e}_n is the unit vector in the direction of n and ∇ is the horizontal gradient operator.

To estimate v' , first note that since the alongshore wind forcing over the California current region negligibly changes the anomalous coastal sea level (Enfield and Allen 1980[3]), the condition of no normal flow at low frequencies implies

$$\frac{g}{f} \mathbf{e}_s \cdot \nabla \eta' = 0, \quad (2.7)$$

where s is the alongshore distance from the origin and \mathbf{e}_s is the unit vector in the direction of s (see Fig. 2.5). Equation (2.7) can also be written

$$\mathbf{e}_s \cdot (\mathbf{i}\eta'_x + \mathbf{j}\eta'_y) = -\sin \theta \eta'_x + \cos \theta \eta'_y = 0, \quad (2.8)$$

where \mathbf{i} is the unit eastward vector, \mathbf{j} the unit northward vector and θ is the angle of the coastline with due north (see Fig. 2.5). It follows from (2.6) that

$$v' = \frac{g}{f} \mathbf{e}_n \cdot \nabla \eta' = \frac{g}{f} \mathbf{e}_n \cdot (\eta'_x \hat{i} + \eta'_y \hat{j}) \quad (2.9)$$

,i.e.,

$$v' = \frac{g}{f} (\eta'_x \cos \theta + \eta'_y \sin \theta). \quad (2.10)$$

Using (2.8), Eq. (2.10) can be written

$$v' = \frac{g}{f} \eta'_x \cos \theta [1 + (\tan \theta)^2] = \frac{g}{f \cos \theta} \eta'_x \quad (2.11)$$

or, by (2.5),

$$v' = \frac{g}{f \gamma \cos \theta} \frac{\partial \eta'}{\partial t}. \quad (2.12)$$

Notice that (2.12) enables us to estimate the anomalous large-scale low-frequency interannual surface flows anywhere in the California current using the time derivative of local interannual sea level. Since local sea level is related to coastal San Diego sea level by westward wave propagation, large-scale interannual variations in the California current can be estimated by appropriately lagging the time derivative of interannual San Diego sea level.

It is clear from (2.12) that alongshore anomalous California current variability is directly linked to San Diego sea level and hence to climate variability associated with El Niño. Why, then, did Schneider et al. (2005)[17] find that the anomalous California current variability is unrelated to large-scale climate indices? The correlation of coastal v' with San Diego sea level is proportional to the covariance of coastal v' and η' , which, by (2.12), is proportional to the covariance of v' and $\frac{\partial \eta'}{\partial t}$. The latter covariance is

$$\lim_{T \rightarrow \infty} T^{-1} \int_0^T \eta' \frac{\partial \eta'}{\partial t} dt = \lim_{T \rightarrow \infty} \frac{1}{T} \left[\frac{1}{2} (\eta'^2) \right]_0^T. \quad (2.13)$$

since (η'^2) is always finite. Thus coastal v' is uncorrelated with San Diego interannual sea level and therefore, not surprisingly, with the El Niño index NIÑO3.4.

Consequently, even though v' is directly related to the San Diego and ENSO signals through (2.12), it is uncorrelated with those signals because it is proportional to $\frac{\partial \eta'}{\partial t}$ rather than η' . This proportionality is entirely due to the propagating nature of the signal. Representation of v' using the first EOF mode of dynamic height anomalies (see Chelton et al. 1982[4]) does not represent $\frac{\partial \eta'}{\partial t}$ and therefore does not model v' .

Closely associated with the alongshore current anomaly is the anomalous alongshore particle displacement $(\Delta s)'$. Assuming, as the observations seem to suggest, that the large-scale interannual dynamics are linear, we may write

$$v' = \frac{d}{dt}(\Delta s)'. \quad (2.14)$$

Substituting (2.14) into (2.12) and integrating with respect to time gives

$$(\Delta s)' = \frac{g}{f\gamma \cos \theta} \eta'. \quad (2.15)$$

For typical $\eta' = \pm 5\text{cm}$ (see Fig. 1.2), $g = 9.8\text{m/s}^{-2}$, $\gamma = 4.2\text{cm/s}$ (see Fig. 2.3), and $\theta = 46^\circ$, the anomalous alongshore displacement $(\Delta s)' = \pm 210\text{km}$, i.e., the range of particle displacement alongshore due to interannual flow is about 400 km. The corresponding anomalous velocity, $(\Delta s)'\omega$, where ω is a typical ENSO frequency, is only about 1 to 2 cm/s. Physically, even though the velocity is small, the alongshore displacement is large because the current is in one direction for a long time.

2.6 Interannual fluctuations in California Current zooplankton

Chelton et al. (1982)[5] showed that interannual fluctuations in the California current zooplankton were not related to variations in the local wind forcing but rather to variations in the California current. They suggested that when the sea level is anomalously low, the California current is stronger than normal and advects the higher nutrient northern water southward. The higher nutrient water then results in increased phytoplankton and zooplankton. But Roesler and Chelton (1987)[18], by examining the age distribution of the zooplankton, concluded that in the CalCOFI region of interest (see Fig. 2.1), the interannual changes in zooplankton were mainly due to interannual advection of the zooplankton themselves. However, this conclusion was based on limited data.

The hypothesis of Roesler and Chelton can be written mathematically as

$$\frac{\partial n'}{\partial t} = -v' \frac{\partial \bar{n}}{\partial s}, \quad (2.16)$$

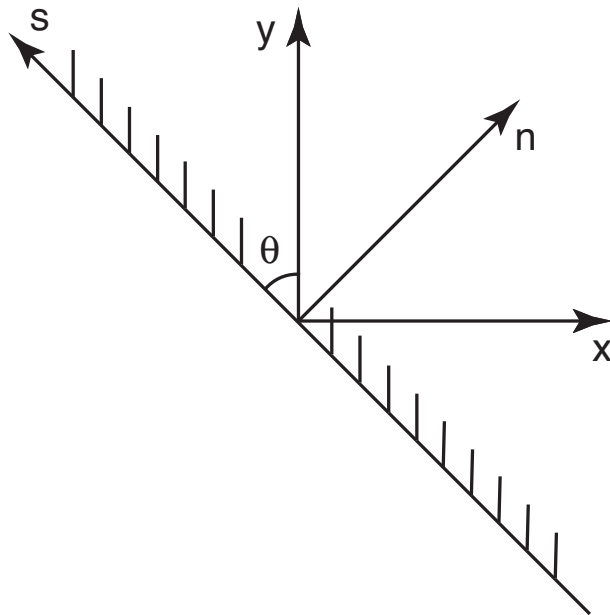


Figure 2.5: Normal and tangential coordinates (n,s) to a coastline making an angle θ with due north.

where n' is the anomalous interannual zooplankton concentration and $\frac{\partial \bar{n}}{\partial s}$ is the mean alongshore gradient in zooplankton. From (2.16), (2.14) and an integration with respect to time,

$$n' = -(\Delta s)' \frac{\partial \bar{n}}{\partial s}, \quad (2.17)$$

with $(\Delta s)'$ given by (2.15). In our region of interest (Fig. 2.1), $\frac{\partial \bar{n}}{\partial s} \approx 20ml/1000m^3$ per 100 km alongshore and typical $(\Delta s)' \approx 200km$ giving typical $n' = 40ml/1000m^3$. This is a factor of 5 or so too small compared with observations. In addition, from (2.15) and (2.17), n' should be proportional to η' . However, the observed correlation between n' and η' averaged over the CalCOFI region is 0.54 whereas the correlation between $\ln n'$ and η' is 0.64 (see Fig. 2.6). It therefore seems unlikely that the anomalous advection of zooplankton

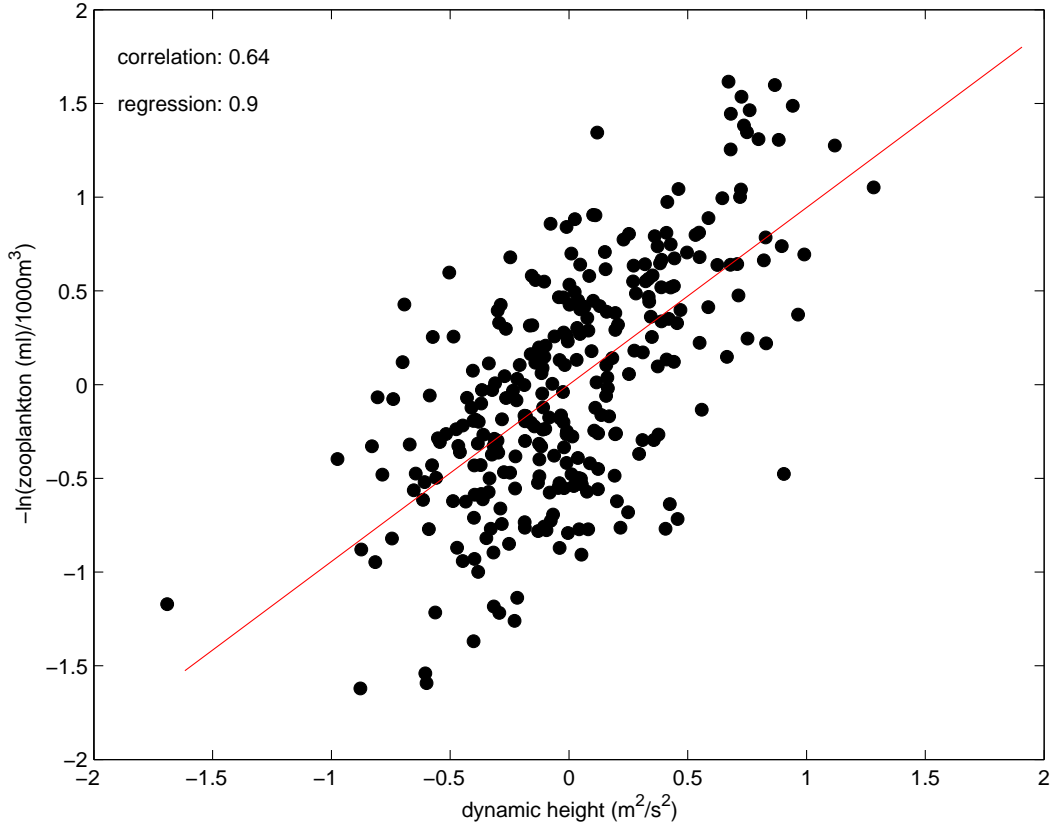


Figure 2.6: Monthly anomalies of the logarithm of zooplankton volume concentration averaged over the CalCOFI region plotted against anomalies of the dynamic height averaged over the CalCOFI region. The correlation coefficient is 0.64 and the regression coefficient, 0.9 with an error of 0.3 at a confidence level of 90%.

explains the observed zooplankton anomaly.

Another possible mechanism, one that also predicts that $\ln n'$ is proportional to η' , is similar to that proposed by Clarke and Li (2004)[15] and Li and Clarke (2004)[24]. Specifically, if the sea level rises by an amount $\delta\eta$, then, by the arguments in section 2.5 (see, e.g., (2.15)), there is northward alongshore particle displacement and a lower nutrient concentration locally. In addition, positive $\delta\eta$ corresponds to a downward displacement of the pycnocline and nutricline, also resulting in a lower nutrient concentration. A lower nutrient concentration will lead to fewer phytoplankton and fewer zooplankton. We expect that larger $\delta\eta$ will result in a bigger change δn in zooplankton concentration and we crudely model this by assuming that δn is proportional to $\delta\eta$. We also suspect that δn will be proportional to

n because the same nutrient change will result in more biomass if there are more animals present. Thus we write

$$\delta n = -\lambda n \delta \eta, \quad (2.18)$$

the negative sign being included because we take $\lambda > 0$ and an increased (decreased) sea level results in negative (positive) δn . Integrating (2.18) from a sea level η_0 when $n = n_0$ to general η and n gives

$$\ln \frac{n}{n_0} = -\lambda (\eta - \eta_0). \quad (2.19)$$

Subtracting the mean and annual cycle from both sides of (2.19) gives the anomaly equation

$$(\ln n)' = -\lambda \eta'. \quad (2.20)$$

The relationship (2.20) applies locally but cannot be tested point by point because the zooplankton data are too noisy locally. If we average the $(\ln n)'$ over the entire CalCOFI region, then from (2.20) we might expect $(\ln n)'$ to be proportional to $-\eta'$ averaged over the region. As noted earlier, Fig. 2.6 shows that these time series are indeed correlated ($r = 0.64$). Since also (2.20) supposedly applies locally, and propagates westward from the coast, $(\ln n)'$ averaged over the CalCOFI region should lag the sea level at the coast. The observed lag of η' at the westernmost part of the CalCOFI region is about 6 months (see Fig. 2.3), so the lag of $(\ln n)'$ averaged over the CalCOFI region should be about 3 months. Consistent with this, Fig. 2.7 shows that the San Diego sea level anomaly is most highly correlated with the anomalous logarithm of the zooplankton concentration when it leads it by about 2 months. This implies that the zooplankton concentration in the California current can be monitored and predicted using monthly San Diego sea level.

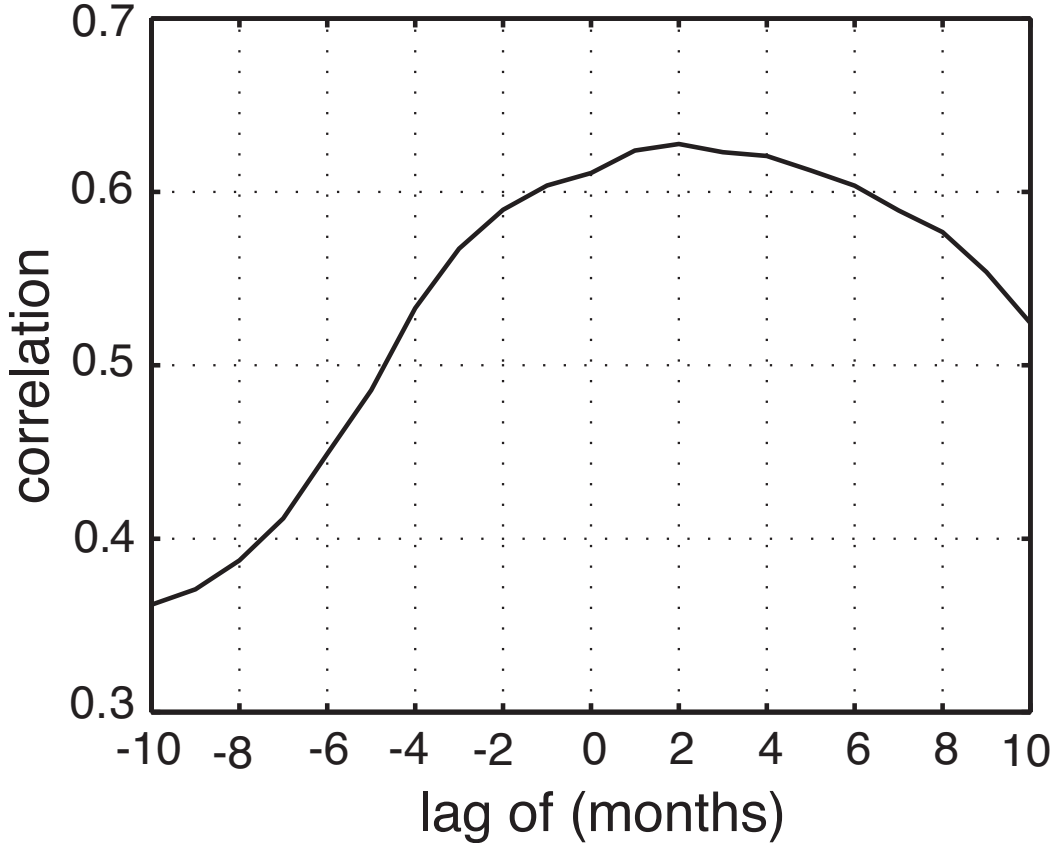


Figure 2.7: Lagged correlation of interannual $\ln n$ averaged over the CalCOFI region with monthly anomalous negative San Diego sea level (η'). A positive lag means η leads $\ln n$.

2.7 Concluding remarks

Both hydrographic and altimeter observations indicate a definite westward propagation of sea level and dynamic height anomalies off the California coast. However, the westward propagation speed of about 4.2 cm/s is approximately double the standard long Rossby wave speed of 2.2 cm/s. Inclusion of the mean California current in the theory (Killworth et al. 1997[12]) increases rather than decreases the discrepancy. When both bottom topography and mean flow are included (Killworth and Blundell 2002[16]), the propagation speed increases but it is still only about half that observed.

The large scale westward propagation fundamentally affects the low-frequency flow variability. The observations suggest that, because of the propagation, large-scale interannual

current fluctuations in the California current can be approximately monitored using the time derivative of interannual San Diego sea level. Both alongshore and vertical particle displacements change the nutrient content of the surface waters, in both cases an abnormally high sea level corresponding to decreased nutrient concentration in the surface water and an abnormally low sea level to increased nutrient concentration in the surface water. We can expect the nutrient changes to influence the phytoplankton and hence zooplankton population. As shown in section 2.6, this links the anomaly of the logarithm of zooplankton population with monthly sea level anomalies and enables the monitoring and prediction of California current zooplankton population using San Diego sea level.

CHAPTER 3

ROSSBY WAVE, EVAPORATION AND THE INTERANNUAL AND DECADEAL VARIABILITY OF SALINITY AND TEMPERATURE OFF CALIFORNIA

3.1 Introduction

As discussed in chapters 1 and 2, usually during El Niño events California sea level and SST are higher than normal and the thermocline deepens, while during La Niña events, sea level and SST are usually lower and the thermocline shoals. Although this remote forcing explains much of the California coast interannual sea level and SST, it does not explain low-frequency surface salinity since the latter is not well correlated with El Niño indexes (Schneider et al. 2005[17]). This is at least partly due to surface salinity having a large interdecadal component not associated with the interannual El Niño/La Niña cycles. Chelton et al. (1982)[5] suggested that both anomalous alongshore and vertical advection of salt may contribute to the low-frequency variability of salinity. Applying the alongshore advection hypothesis, Schneider et al. (2005)[17] suggested that near-surface salinity anomalies at a hydrographic cross section off Long Beach, California, are due to an accumulation of salt caused by advection of the main meridional salinity gradient by anomalies in the alongshore velocity. Schneider et al. (2005)[17] reproduced a time series of salinity using a model based on the alongshore advection of salt and an ad hoc dilution factor. However, the correlation coefficient between model and observed time series was a modest 0.41.

The main goal of this chapter is to answer the following two questions. First, how, dynamically, does the interannual remote signal cause the observed interannual variability in temperature and, to some extent, in salinity? Second, why does surface salinity have a

large interdecadal component while SST variability is mainly interannual?

To understand the low-frequency salinity and temperature fluctuations, we must first understand the anomalous low-frequency flow. After discussing the low-frequency currents and their connection to long, westward propagating waves in 3.2, section 3.3 uses the high correlation between dynamic height anomalies and temperature anomalies in a sloping mean density field to estimate, empirically, a vertical mode. Still in section 3.3, the empirical mode and the first baroclinic mode are compared at the surface and the vertical and horizontal advection are analysed based on the dynamics of the vertical mode. A model to understand low-frequency salinity anomalies and its physics is developed based on the empirical vertical mode and evaporation in section 3.4. In section 3.5, the model predictions and the observations are compared. A concluding section 3.6 summarizes the main results.

3.2 Westward propagating low-frequency waves and their currents

3.2.1 Low-frequency currents beneath the surface

In chapter 2 the anomalous low-frequency flow at the surface was analyzed (Eq. (2.12)). But here we will need anomalous alongshore and vertical velocities throughout the water depth. It will be assumed that the anomalous pressure is given by:

$$p' = F(z)\rho_*g\eta', \quad (3.1)$$

where the function F , whose structure will be determined empirically, is unity at the surface since p' , the anomalous pressure, is $\rho_*g\eta'$ there. By geostrophy, the anomalous alongshore velocity v' is

$$v' = \frac{1}{\rho_*f} \frac{\partial p'}{\partial n} = \frac{g}{f} \frac{\partial \eta'}{\partial t} F(z), \quad (3.2)$$

or, using equation (2.12),

$$v' = \frac{g}{\gamma f \cos \theta} \frac{\partial \eta'}{\partial t} F(z). \quad (3.3)$$

To obtain an expression for w' , begin with the incompressibility condition that following particles the density does not change. The anomaly version of this condition in terms of the anomalous density ρ' linearized about mean conditions is

$$\frac{\partial \rho'}{\partial t} + \bar{u} \frac{\partial \rho'}{\partial n} + u' \frac{\partial \bar{\rho}}{\partial n} + \bar{v} \frac{\partial \rho'}{\partial s} + v' \frac{\partial \bar{\rho}}{\partial s} + \bar{w} \frac{\partial \rho'}{\partial z} + w' \frac{\partial \bar{\rho}}{\partial z} = 0, \quad (3.4)$$

where here and elsewhere in this paper the overbar refers to a time mean. Using the westward propagating wave estimate (equation (2.4)),

$$\frac{\partial \rho'}{\partial t} = \gamma \frac{\partial \rho'}{\partial x} = \gamma \cos \theta \frac{\partial \rho'}{\partial n} \quad (3.5)$$

we see that the second term on the left hand side of (3.4) is negligible provided that $|u| \ll 3$ cm/s. Since the California current has a speed of about 5 cm/s and is nearly parallel to the coast, $|\bar{u}| \ll 3$ cm/s and $\bar{u} \frac{\partial \rho'}{\partial n}$ is negligible in (3.4). Also, observed $\frac{\partial \bar{\rho}}{\partial n} \sim \frac{\partial \bar{\rho}}{\partial s}$ but, from low-frequency dynamics near eastern ocean boundaries, $|u'| \ll |v'|$ (see, e.g., Clarke and Shi 1991) so the third term on the left hand side of (3.4) can be neglected compared with the fifth term. Since also $w' \sim \bar{w}$ (see plate 4 of Bograd et al. 2001[25]) and $\left| \frac{\partial \rho'}{\partial z} \right| \ll \left| \frac{\partial \bar{\rho}}{\partial z} \right|$, $\bar{w} \frac{\partial \rho'}{\partial z}$ is negligible compared with $w' \frac{\partial \bar{\rho}}{\partial z}$. Finally, although $\bar{v} \sim 5$ cm/s and $v' \sim 1$ cm/s, $\left| \frac{\partial \rho'}{\partial s} \right|$ is of order 1% of $\left| \frac{\partial \bar{\rho}}{\partial s} \right|$ and so $\frac{\partial \rho'}{\partial s}$ is negligible compared with $v' \frac{\partial \bar{\rho}}{\partial s}$. Under these approximations (3.4) reduces to

$$\frac{\partial \rho'}{\partial t} + v' \frac{\partial \bar{\rho}}{\partial s} + w' \frac{\partial \bar{\rho}}{\partial z} = 0. \quad (3.6)$$

This equation may also be written as

$$w' = v' \phi - \frac{\partial \rho' / \partial t}{\partial \bar{\rho} / \partial z}, \quad (3.7)$$

where

$$\phi = -\frac{\partial \bar{\rho} / \partial s}{\partial \bar{\rho} / \partial z} \quad (3.8)$$

is the slope that a constant density surface makes with the horizontal in a vertical/alongshore plane. Since this slope is very small, ϕ is an excellent approximation of the angle between the horizontal and the constant density surface in the vertical/alongshore plane. Equation (3.7) shows that the anomalous vertical velocity is partly due to particles sliding parallel to isopycnals ($v'\phi$) and partly due to particles crossing isopycnals ($\frac{\partial \rho' / \partial t}{\partial \bar{\rho} / \partial z}$).

To find w' terms of η' , we use the hydrostatic balance

$$\frac{\partial p'}{\partial z} = -g\rho' \quad (3.9)$$

and (3.1) to obtain

$$\rho' = -\frac{dF}{dz} \rho_* \eta'. \quad (3.10)$$

Substitution of (3.10) and (3.3) into (3.7) then gives

$$w' = g \frac{\partial \eta'}{\partial t} \left(\frac{\phi}{\gamma f \cos \theta} F - \frac{1}{N^2} \frac{dF}{dz} \right), \quad (3.11)$$

where N is the buoyancy frequency defined by

$$N^2 = -\frac{g}{\rho_*} \frac{\partial \bar{\rho}}{\partial z}. \quad (3.12)$$

3.3 Estimation of the vertical function $F(z)$

3.3.1 Correlation between anomalies of temperature and dynamic height

Observed anomalous temperature time series were obtained in the same way as dynamic height in chapter 2. Initially, the 63 stations of the CalCOFI data set are binned in 6

alongshore regions based on the distance from the coast (Fig. 2.1). For each standard depth at each month where data were available, the temperature was averaged over the region, resulting in 6 monthly time series at each depth. Anomalies are formed by subtracting the 12 calendar month estimate of the mean annual cycle for each of the 6 regions and for each depth. Then the time trend in each temperature time series was removed. For each of the 6 regions, the anomalous temperature time series at each depth was correlated with the anomalous dynamic height and the correlation and regression coefficients recorded.

The correlation in the first 200 meters is high (see Fig.3.1), with the maximum correlation between 50 and 100 meters, depending on the region. The regression coefficients (Fig. 3.2) are smaller in water deeper than 200 meters, indicating much smaller variability there. The correlation (Fig 3.1) is also usually less beneath 200 meters, consistent with a lower signal and, therefore, lower signal to noise ratio. The correlation falls towards the surface. In this case heat flux anomalies through the surface, giving rise to another temperature signal not correlated with η' , may be the reason for this correlation fall.

However, the above results indicate a strong link between the sea-level and the temperature for, at least, the upper 200 meters. This link will be used below to estimate the empirical mode $F(z)$ at the upper 200 meters of the water column.

3.3.2 Linking anomalies of temperature and dynamic height theoretically

Assuming that the anomalous form of the temperature conservation equation is (cf (3.4))

$$\frac{\partial T'}{\partial t} + \bar{u} \frac{\partial T'}{\partial n} + u' \frac{\partial \bar{T}}{\partial n} + \bar{v} \frac{\partial T'}{\partial s} + v' \frac{\partial \bar{T}}{\partial s} + \bar{w} \frac{\partial T'}{\partial z} + w' \frac{\partial \bar{T}}{\partial z} = 0. \quad (3.13)$$

By similar arguments to those used for density anomalies, (3.13) can be simplified to

$$\frac{\partial T'}{\partial t} + v' \frac{\partial \bar{T}}{\partial s} + w' \frac{\partial \bar{T}}{\partial z} = 0. \quad (3.14)$$

Substituting the expressions for v' and w' given by equations (3.3) and (3.11) into equation (3.14), we have

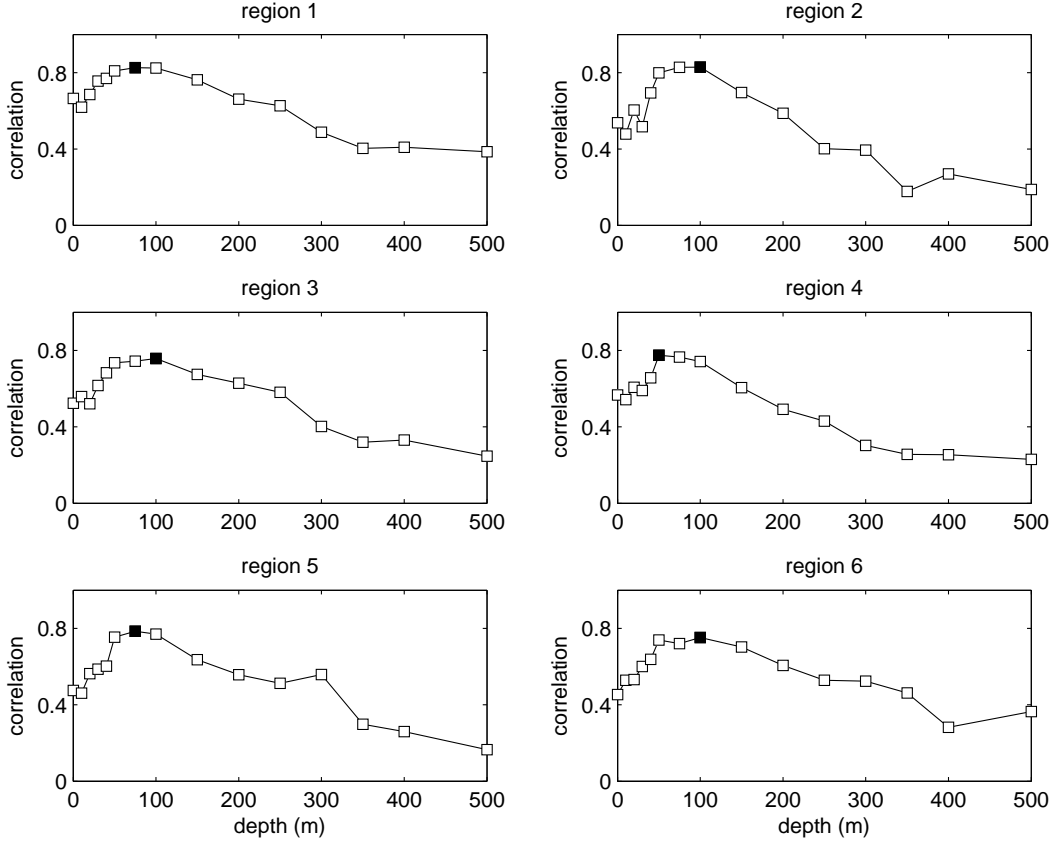


Figure 3.1: Correlation coefficients between anomalies of temperature and anomalies of dynamic height. The solid square represents the maximum correlation in the first 500 meters. The regions are separated according to Fig. 2.1.

$$\frac{\partial T'}{\partial t} = -\frac{g}{\gamma f \cos \theta} \frac{\partial \eta'}{\partial t} F(z) \frac{\partial \bar{T}}{\partial s} - g \frac{\partial \eta'}{\partial t} \left(\frac{\phi}{\gamma f \cos \theta} F - \frac{1}{N^2} \frac{dF}{dz} \right) \frac{\partial \bar{T}}{\partial z}. \quad (3.15)$$

Integrating from a time of zero anomaly conditions ($T' = \eta' = 0$) to some general time t gives

$$T' = \nu \eta', \quad (3.16)$$

with the theoretical regression coefficient ν given by

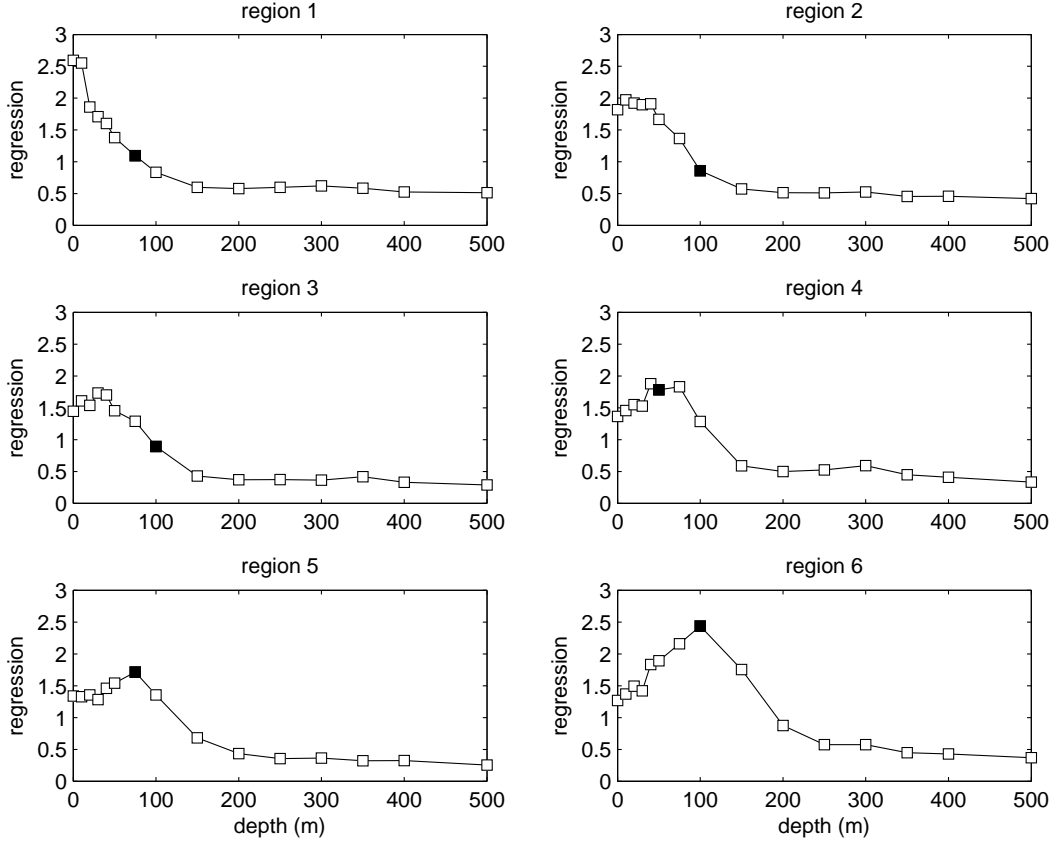


Figure 3.2: Regression coefficients between anomalies of temperature and anomalies of dynamic height. The solid square represents the maximum correlation in the first 500 meters. The regions are separated according to Fig. 2.1.

$$\nu = -\frac{g}{\gamma f \cos \theta} F(z) \frac{\partial \bar{T}}{\partial s} - g \left(\frac{\phi}{\gamma f \cos \theta} F - \frac{1}{N^2} \frac{dF}{dz} \right) \frac{\partial \bar{T}}{\partial z}. \quad (3.17)$$

The expression for ν can also be written

$$\nu = -g \left[\frac{1}{\gamma f \cos \theta} (\phi_T - \phi) F + \frac{1}{N^2} \frac{dF}{dz} \right] \frac{\partial \bar{T}}{\partial z}, \quad (3.18)$$

where ϕ_T , defined by $-\frac{\partial \bar{T}/\partial s}{\partial \bar{T}/\partial z}$, is the slope that a constant temperature surface makes with the horizontal in a vertical/alongshore plane.

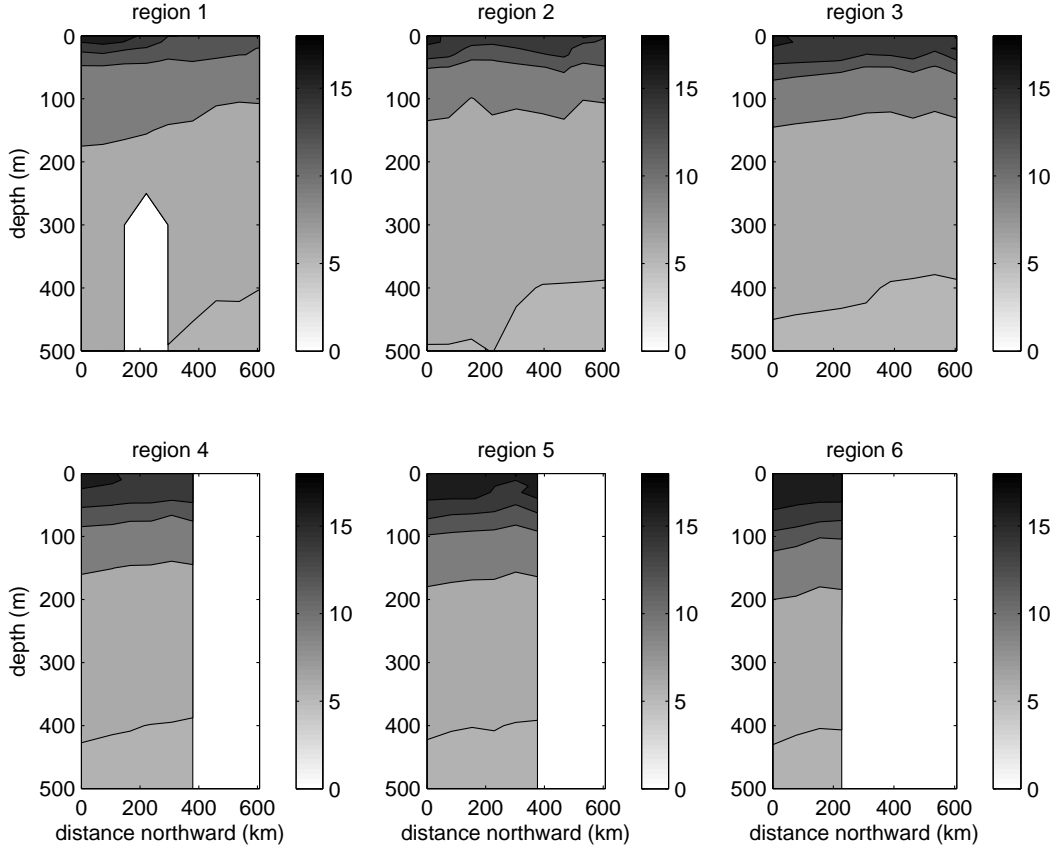


Figure 3.3: Temporally averaged temperature for the whole CalCOFI record at the 6 binned CalCOFI regions (see Fig. 2.1). The isotherm slopes are generally positive toward the north.

3.3.3 Estimating $F(z)$ numerically

The empirical vertical mode can be easily estimated by discretization of equation (3.18) assuming that

$$\frac{dF}{dz} = \frac{F^{n+1} - F^n}{\Delta z}, \quad (3.19)$$

with F^0 being the value of F at the surface.

Following a standard numerical approach, substitution of F by F^n and equation (3.19) into equation (3.18) gives

$$F^{n+1} = \left[1 - \frac{N^2 g}{\gamma f \cos \theta} (\phi_T - \phi) \Delta z \right] F^n - \frac{\nu N^2 \Delta z}{\partial \bar{T} / \partial z}, \quad (3.20)$$

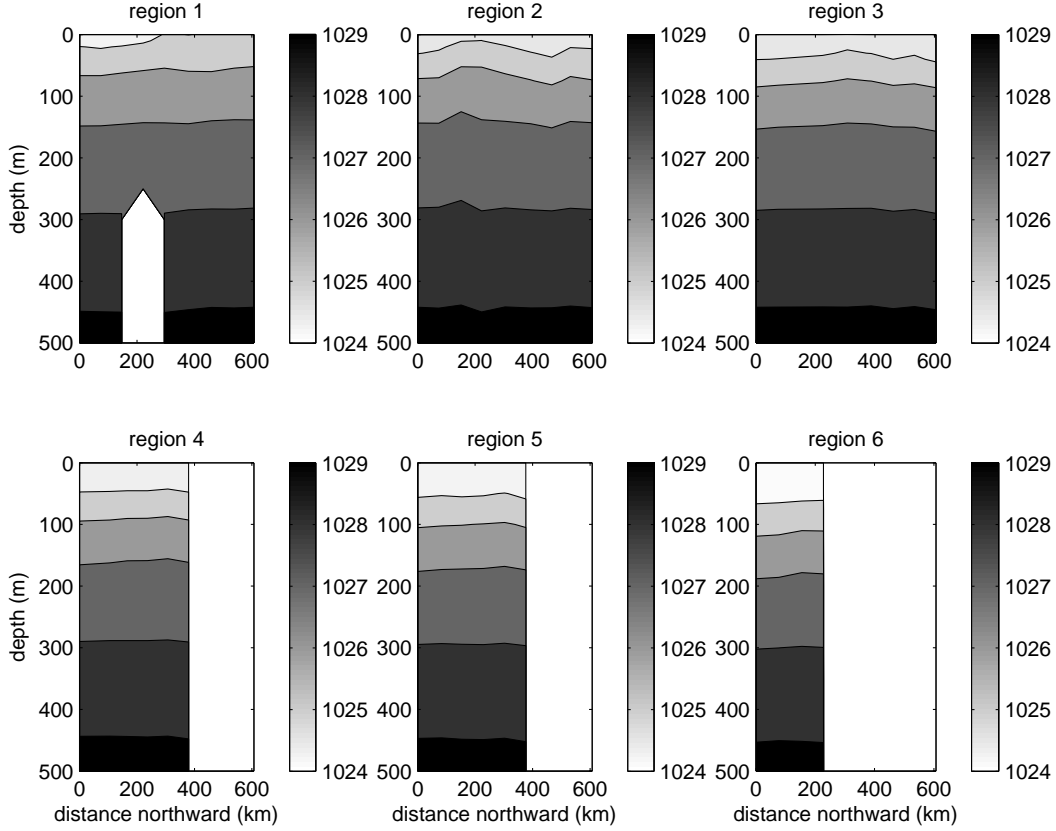


Figure 3.4: Temporally averaged density for the whole CalCOFI record at the 6 binned CalCOFI regions (see Fig. 2.1). The pycnocline slopes are generally positive toward the north.

with $n = 0, 1, 2, \dots, M$ from surface to bottom. Since we need $p' = \rho_* g \eta'$ at the surface, equation (3.1) gives $F^0 = 1$ and, therefore, equation (3.20) can be integrated from the surface to the bottom.

The vertical-alongshore structures of temperature and density used to estimate the empirical vertical modes are shown in Fig. 3.3 and Fig. 3.4. The profiles of N^2 are shown Fig. 3.5. The empirical vertical modes are discussed in the next section.

3.3.4 The Empirical modes

Initially, it's very clear that the empirical modes are very similar for all regions, although the regression coefficients are relatively different. The results are shown in Fig. 3.6 and the empirical modes were calculated for the top 200 meters only, where the correlation between

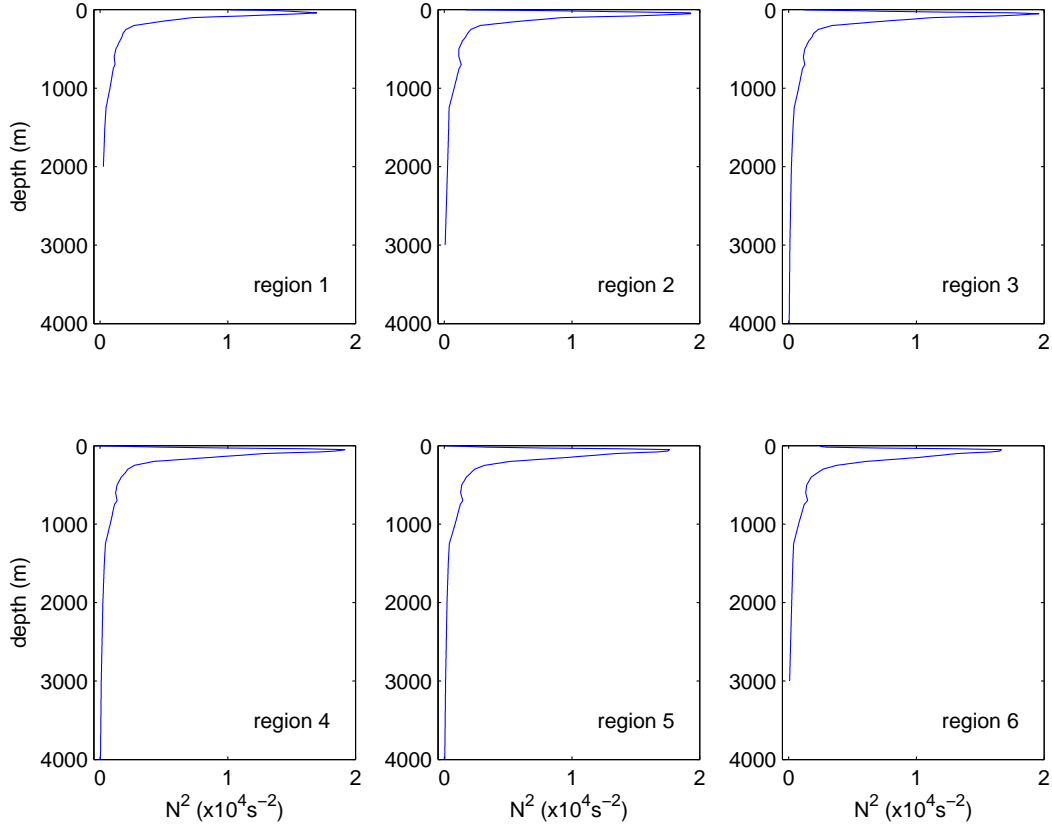


Figure 3.5: Temporally averaged N^2 for the whole CalCOFI record at the 6 binned CalCOFI regions (see Fig. 2.1).

temperature and dynamic height is higher.

Comparing the empirical modes with the first baroclinic mode obtained with profiles of temperature and salinity provided by NODC-WOA98 by the NOAA/OAR/ESRL PSD, Boulder, Colorado, USA, from their Web site at <http://www.cdc.noaa.gov/> (Fig. 3.7), we first note a relatively similar shape between the first vertical mode and the empirical modes. It's also clear that the vertical derivative of the empirical mode is relatively stronger, in the average, than the derivative of the first baroclinic mode. Close to the surface this difference seems to be enhanced. This suggests a relatively different dynamics from the standard theory induced by a non-horizontal pycnocline. This is not a surprise once the the standard theory (see, e.g., Gill and Clarke (1974)[26]) assumes that the horizontal advection of density is negligible when compared with the vertical advection of density. However, using standard

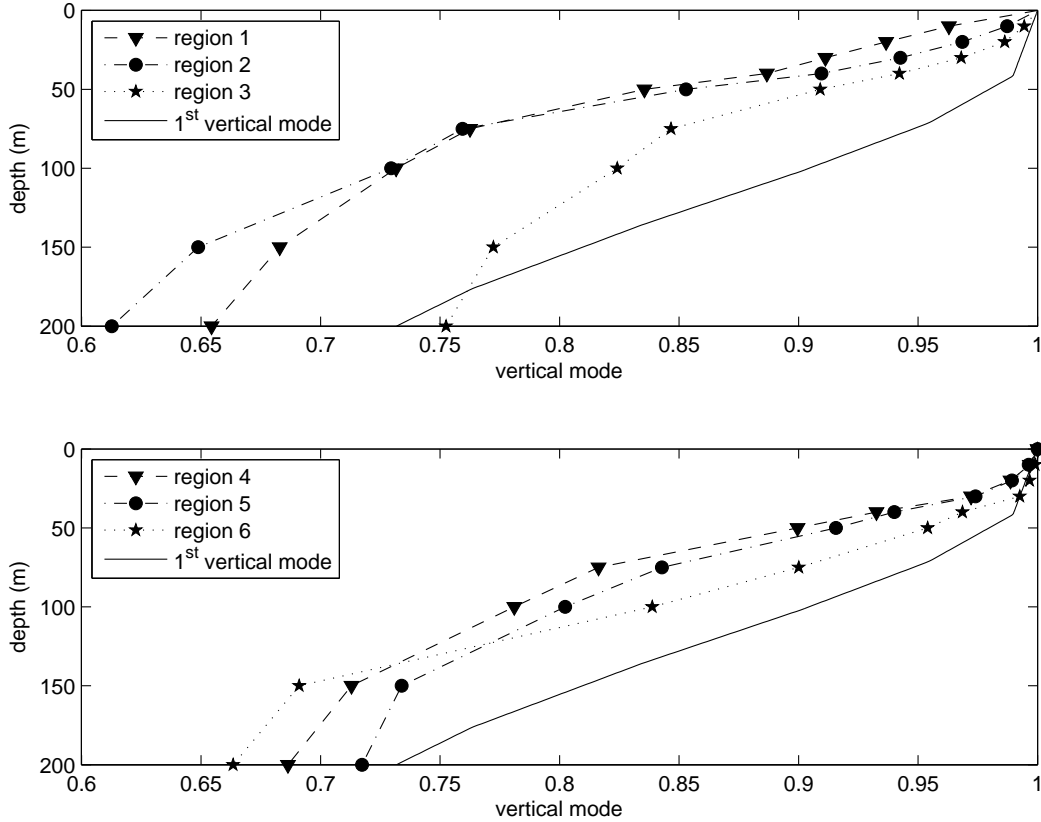


Figure 3.6: Vertical empirical modes $F(z)$ obtained from equation (3.17) and the regression coefficients shown in Fig. 3.2. The empirical modes are only calculated from the surface up to 200 meters deep, where the correlation is relatively high, assuming that the vertical modes are unity at the surface.

values of vertical and horizontal velocities and density gradients obtained from the CalCOFI data set, the horizontal advection is comparable to the vertical advection in the region near the surface.

3.3.5 Particle displacements

If we let Y' be the anomalous alongshore particle displacement, then

$$\frac{dY'}{dt} = v'. \quad (3.21)$$

Substitution of (3.3) into the above equation and integrating once with respect to time gives

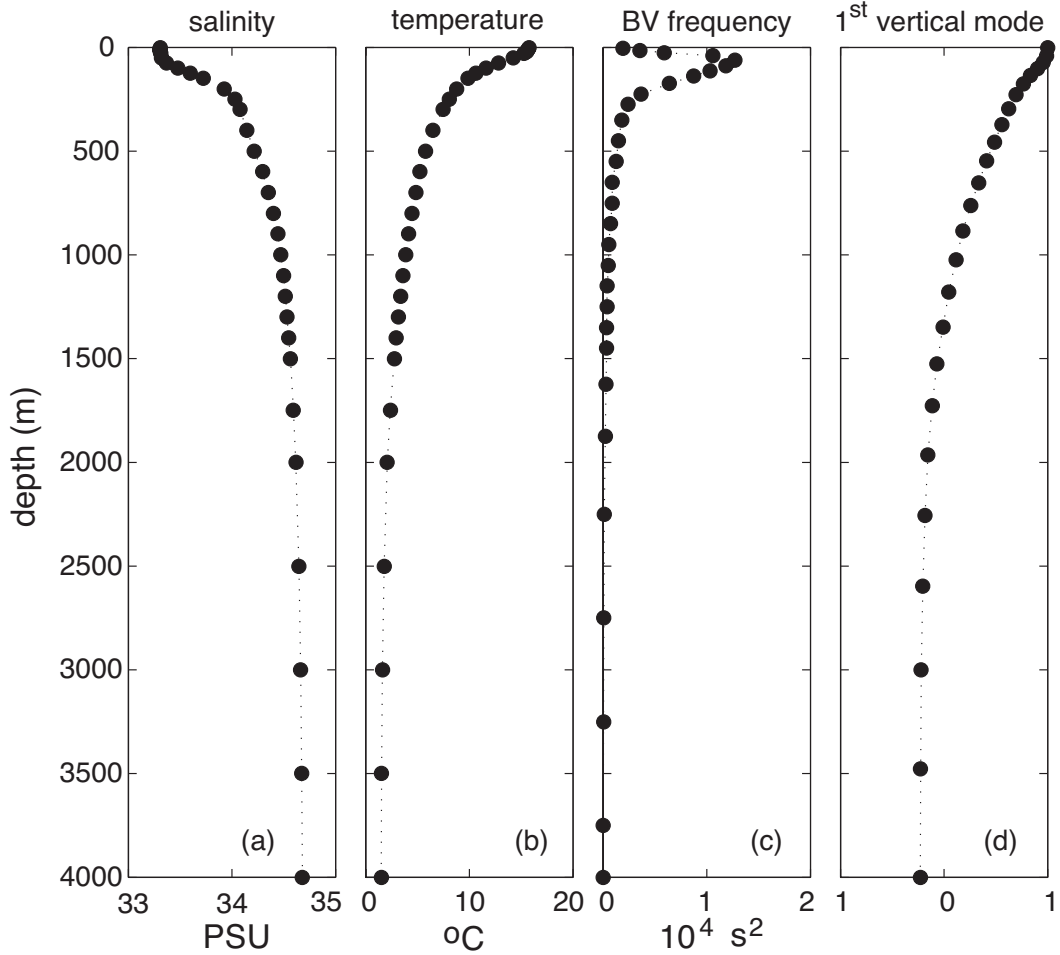


Figure 3.7: Average (a) salinity, (b) temperature and (c) Brunt-Vaisala frequency for the CalCOFI region using NODC-World Ocean Atlas Data (website address <http://www.cdc.noaa.gov/cdc/data.nodc.woa98.html>). The first vertical mode profile (d) calculated using the data in (c).

$$Y' = \frac{g}{\gamma f \cos \theta} \eta' F, \quad (3.22)$$

i.e., the anomalous alongshore particle displacement is northward for $\eta' > 0$ and southward for $\eta' < 0$. Similarly, we can define Z' to be the upward vertical displacement so

$$\frac{dZ'}{dt} = w' \quad (3.23)$$

and, using (3.11) and an integration with respect to time gives

$$Z' = g \left[\frac{\phi}{\gamma f \cos \theta} F - \frac{1}{N^2} \frac{dF}{dz} \right] \eta'. \quad (3.24)$$

Calculations show that the term in square brackets is negative in the CalCOFI region. In other words, when η' is (say) positive the particle displacement is negative. This is what we normally expect for vertical motion in the upper ocean, when the sea level rises, the thermocline deepens.

From the above results for particle displacements, we see that both vertical and alongshore displacements act in the same sense to induce temperature anomalies. For example, if the sea level anomaly is positive, the alongshore displacement is northward, carrying warmer water northward and locally inducing a positive temperature anomaly. At the same time a positive sea level anomaly induces $Z' < 0$, bringing warmer water downward and, again, locally inducing a positive temperature anomaly.

3.4 Salinity anomalies

3.4.1 Low-frequency salinity beneath a surface layer

Over a surface layer about 50-100 m thick the salinity in the CalCOFI region hardly varies with depth (see, e.g., Fig. 4 of Schneider et al. 2005[17]). The salinity in this surface layer is subject to change via surface fluxes of fresh water through evaporation, precipitation and runoff from the land. But beneath this layer we expect the salinity S to be conserved following the flow so there

$$\frac{DS}{Dt} = 0. \quad (3.25)$$

Linearizing this equation for low frequency perturbations about the mean gives, very similarly to temperature,

$$\frac{\partial S'}{\partial t} + \bar{u} \frac{\partial S'}{\partial n} + u' \frac{\partial \bar{S}}{\partial n} + \bar{v} \frac{\partial S'}{\partial s} + v' \frac{\partial \bar{S}}{\partial s} + \bar{w} \frac{\partial S'}{\partial z} + w' \frac{\partial \bar{S}}{\partial z} = 0. \quad (3.26)$$

By similar analysis to that used for density and temperature anomalies, (3.26) can be simplified to

$$\frac{\partial S'}{\partial t} + v' \frac{\partial \bar{S}}{\partial s} + w' \frac{\partial \bar{S}}{\partial z} = 0. \quad (3.27)$$

Substitution of (3.3) and (3.11) into (3.27) gives

$$\frac{\partial S'}{\partial t} = -\frac{g}{\gamma f \cos \theta} \frac{\partial \eta'}{\partial t} F(z) \frac{\partial \bar{S}}{\partial s} - g \frac{\partial \eta'}{\partial t} \left(\frac{\phi}{\gamma f \cos \theta} F - \frac{1}{N^2} \frac{dF}{dz} \right) \frac{\partial \bar{S}}{\partial z}. \quad (3.28)$$

Upon integrating (3.28) once with respect to time from the normal conditions $S' = 0$ when $\eta' = 0$, we have

$$S' = \mu \eta', \quad (3.29)$$

where

$$\mu = -\frac{g}{\gamma f \cos \theta} F(z) \frac{\partial \bar{S}}{\partial s} - g \left(\frac{\phi}{\gamma f \cos \theta} F - \frac{1}{N^2} \frac{dF}{dz} \right) \frac{\partial \bar{S}}{\partial z}, \quad (3.30)$$

or

$$\mu = -g \left[\frac{1}{\gamma f \cos \theta} (\phi_S - \phi) F + \frac{1}{N^2} \frac{dF}{dz} \right] \frac{\partial \bar{S}}{\partial z}. \quad (3.31)$$

In (3.31) ϕ_S , defined by $-\frac{\partial \bar{S}/\partial s}{\partial \bar{S}/\partial z}$, is the slope that a constant salinity surface makes with the horizontal in a vertical/alongshore plane. Figure 3.8 shows that ϕ_S is, in general, negative. Thus beneath about 100 m depth, where (3.27) is valid, the local sea level and salinity anomalies should be highly correlated with a z-dependent regression coefficient μ given by (3.30). Note that the relationship (3.29) and (3.30) is crucially dependent on v' being proportional to $\frac{\partial \eta'}{\partial t}$ (see (3.3)), a relationship that holds because of westward Rossby wave propagation; at higher frequencies motion decays away from the coast (see, e.g., Clarke and Shi 1991[27]) and S' is proportional to η' rather than $\frac{\partial \eta'}{\partial t}$.

A physical interpretation of (3.29) follows by substituting the displacements into (3.27) and then integrating with respect to time to obtain

$$S' = -\frac{\partial \bar{S}}{\partial s} Y' - \frac{\partial \bar{S}}{\partial z} Z', \quad (3.32)$$

where the anomalous alongshore and vertical particle displacements Y' and Z' are given by (3.22) and (3.24). Thus the salinity anomaly S' can be regarded as the sum of a salinity anomaly due to an alongshore displacement $-\frac{\partial \bar{S}}{\partial s} Y'$ and a salinity anomaly due to a vertical displacement $-\frac{\partial \bar{S}}{\partial z} Z'$. Calculations show that these contributions are of opposite sign and that the vertical displacement contribution dominates. Since $\frac{\partial \bar{S}}{\partial z}$ is negative, from (3.32) the salinity anomaly will have the same sign as Z' which, as we have seen in (3.24), is proportional to a negative number times η' . Thus we would expect μ to be negative in (3.30). Physically, when η' is (say) positive, a particle is displaced anomalously downward ($Z' < 0$) carrying less saline water into a region of saltier water, thus locally making a negative salinity anomaly. By a similar argument, when $\eta' < 0$, positive Z' induces a positive salinity anomaly. We will check this prediction with salinity observations in section 3.5.

3.4.2 Low-frequency salinity in the surface layer

In the surface layer salinity can be changed, not only by alongshore and vertical advection, but also by the addition or removal of fresh water at the surface and subsequent mixing. Schneider et al. (2005)[17] estimate that fresh water fluxes due to evaporation, precipitation and river run off are too small to account for the observed changes in surface salinity. However, while precipitation and river run off do indeed generally have no significant influence, calculations here show that evaporation cannot be neglected.

The evaporation rate E is given by

$$E = \rho_a c_E (q_s - q_a) |u_a|, \quad (3.33)$$

where E is the mass of water evaporated from the sea surface per unit area per unit time, ρ_a the density of the air, c_E a dimensionless constant equal to 1.5×10^{-3} , q_a the specific humidity at 10 m above the ocean surface, q_s the saturation specific humidity at the sea surface temperature and $|u_a|$ the wind speed at 10 m height above the sea surface. It follows from (3.33) that the mass of pure water lost by the ocean per unit time for a unit horizontal

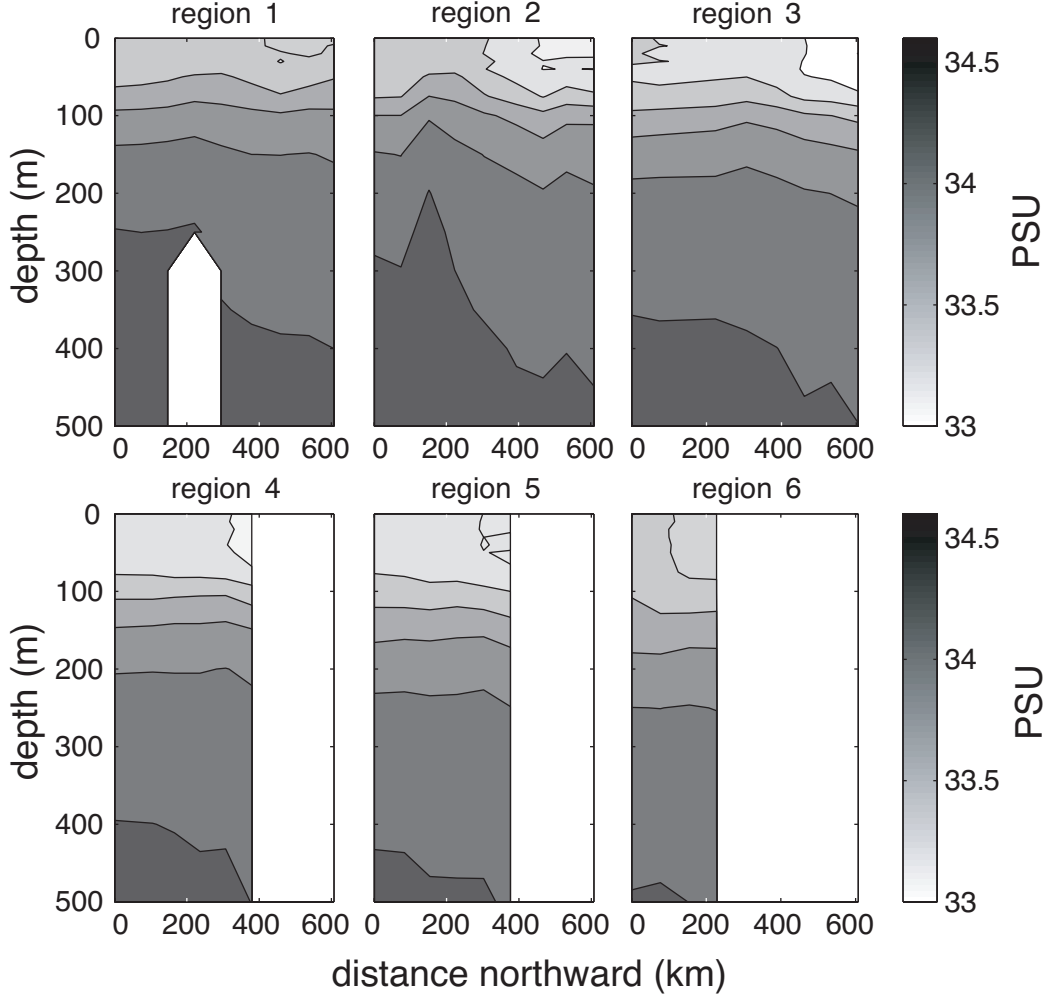


Figure 3.8: Temporally averaged salinity for the whole CalCOFI record at the 6 binned CalCOFI regions (see Fig. 2.1). The isohaline slopes are generally negative toward the north.

area is E . The mass of salt in a surface mixed layer column of height h and unit area is $\rho_* h S$ so in a unit of time the salinity changes by

$$\frac{\rho_* h S}{\rho_* h - E} - \frac{\rho_* h S}{\rho_* h} = \frac{SE}{\rho_* h - E} \approx \frac{SE}{\rho_* h}, \quad (3.34)$$

the second equality in (3.34) following from $E \ll \rho_* h$. Thus if the velocity and salinity vary little vertically over the depth h , the rate of change of S following the motion in the surface layer is

$$\frac{\partial S}{\partial t} + u \frac{\partial S}{\partial n} + v \frac{\partial S}{\partial s} = \frac{SE}{\rho_* h}. \quad (3.35)$$

The linearized anomaly form of this equation is

$$\frac{\partial S'}{\partial t} + \bar{u} \frac{\partial S'}{\partial n} + u' \frac{\partial \bar{S}}{\partial n} + \bar{v} \frac{\partial S'}{\partial s} + v' \frac{\partial \bar{S}}{\partial s} = \frac{\bar{S}E'}{\rho_* h} + \frac{S'\bar{E}}{\rho_* h}. \quad (3.36)$$

The first term on the right hand side is much larger than the second and the left hand side can also be simplified as before (compare (3.26) and (3.27) to get

$$\frac{\partial S'}{\partial t} + v' \frac{\partial \bar{S}}{\partial s} = \frac{\bar{S}E'}{\rho_* h}. \quad (3.37)$$

Upon substituting for using (3.3) and (3.11) and then integrating with respect to time, we have

$$S' = -\frac{g}{\gamma f \cos \theta} \eta' F(z) \frac{\partial \bar{S}}{\partial s} + \frac{\bar{S}}{\rho_* h} \int_0^t E' dt. \quad (3.38)$$

We will test this theoretical prediction in the next section.

3.5 Observed and model salinity anomalies

3.5.1 Testing the advection theory

At each standard depth, from CalCOFI data, 6 time series of anomalous salinity S' were calculated in a similar way to that done for T' and η' except that, since S' did not have a significant trend in time, no trend was removed. According to (3.30), correlation of each S' time series with the corresponding η' time series should be high with regression coefficient μ given by (3.29). Plots of the correlation of S' and η' with depth for each of the 6 zonal distances from the coast (Fig. 3.9) show two regions of low correlation separated by a region of high correlation. The maximum correlation is about 0.8 and deepens with increasing distance from the coast; it is at 100 m deep for regions 1, 2 and 4, 150 m deep for regions

Table 3.1: For each of the 6 regions, the depth of maximum (in magnitude) correlation between observed S' and η' , the value of the correlation coefficient, the corresponding observed regression coefficient with error bars and the regression coefficient expected from theory (see (3.31)).

region	depth of maximum correlation	correlation	regression (observed)	regression (theory)
1	100 m	-0.71	-0.6 ± 0.3	-0.7
2	100 m	-0.86	-1.0 ± 0.4	-0.7
3	100 m	-0.75	-0.8 ± 0.4	-0.6
4	150 m	-0.73	-0.8 ± 0.4	-0.7
5	150 m	-0.79	-0.7 ± 0.4	-0.4
6	200 m	-0.78	-0.7 ± 0.5	-0.5

4 and 5 and at 200 m deep for region 6. Higher correlations are expected when the signal to noise ratio is larger. Consequently the regression coefficient, which is proportional to the salinity signal amplitude according to (3.30), should be maximum at approximately the depths where the correlation is maximum. Figure 3.10 shows that this is indeed the case, with the regression coefficient showing the same qualitative behavior of deepening maximum with increasing distance from the coast. Table 3.1 shows that the observed regression coefficients at maximum (in magnitude) correlation approximately match the theoretical ones. In calculating the theoretical coefficient μ we used $\gamma = 4$ cm/s, from the results in chapter 2, $\theta = 40^\circ$ and f corresponding to latitude 34° N, with $F(z)$ being the empirical vertical mode obtained in section 3.3 (see also Fig. 3.6). Figures 3.9 and 3.10 suggest that the fall in correlation deeper than 100 m - 200 m depth is due to a fall in signal amplitude and hence signal to noise ratio. However, this cannot explain the fall in shallower water than the maximum. In the next section we will suggest that this fall is due to the influence of evaporation.

3.5.2 Testing the theory for low-frequency salinity near the surface

In view of the sparse data, we decided to focus on region 1, the region with easily the most data. The region 1 anomalous salinity data set was very noisy so we filtered in time using an 11-month running mean. Usually many points in the 11-month window were missing but we

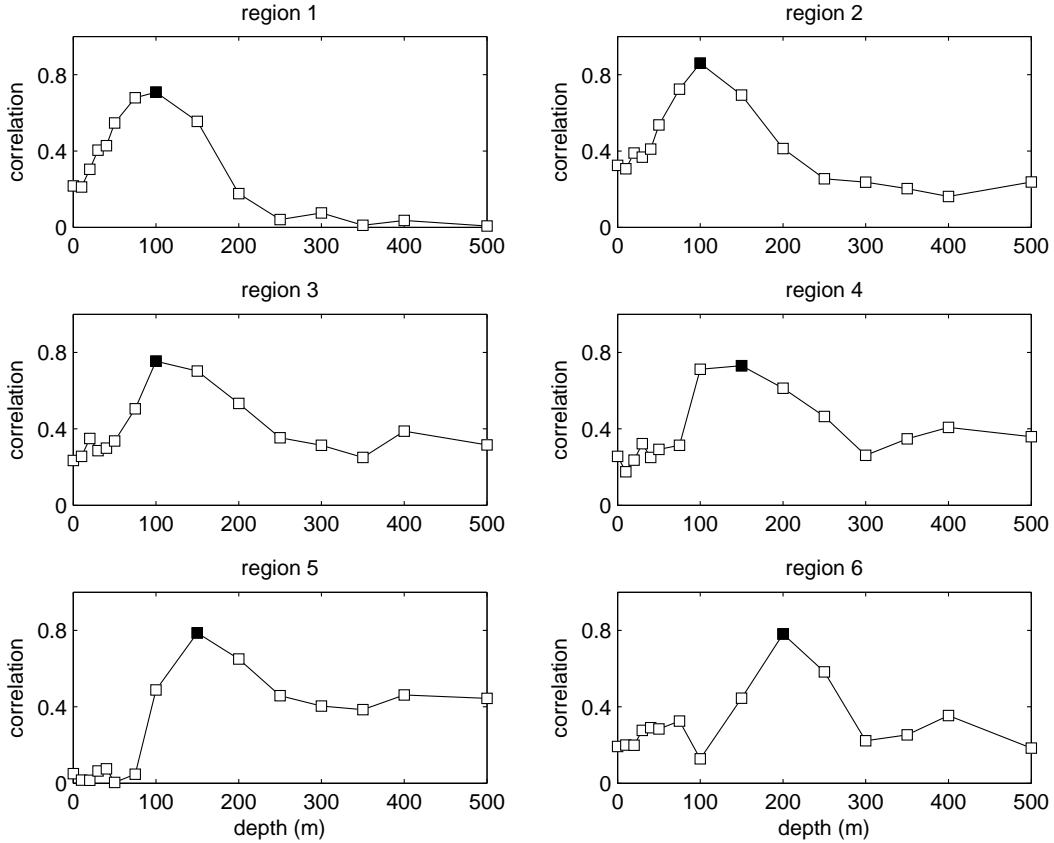


Figure 3.9: Correlation coefficients between anomalies of salinity and anomalies of dynamic height. The solid square represents the maximum correlation in the first 500 meters. The regions are grouped according to Fig. 2.1.

still recorded a value for a given month by averaging over the data present provided at least 3 months had data. We checked the validity of this time series by comparing it (Fig. 3.11) with the coastal salinity anomaly at the surface and at 5 m depth, these data being provided by the Stephen Birch Aquarium-Museum at the Scripps Institute of Oceanography. The high correlation around 0.85 of the surface coastal salinity and the coastal 5 m depth salinity with the gappy region 1 CalCOFI upper ocean salinity suggests that the gappy region 1 CalCOFI signal is approximately valid and that the coastal salinity measurements can be used to monitor variations of average salinity anomalies seaward of the coast. As has been pointed out by Schneider et al. (2005)[17], and as can be seen in Fig. 3.11, there is considerable interdecadal variability in CalCOFI salinity. This is very different to the anomalous surface

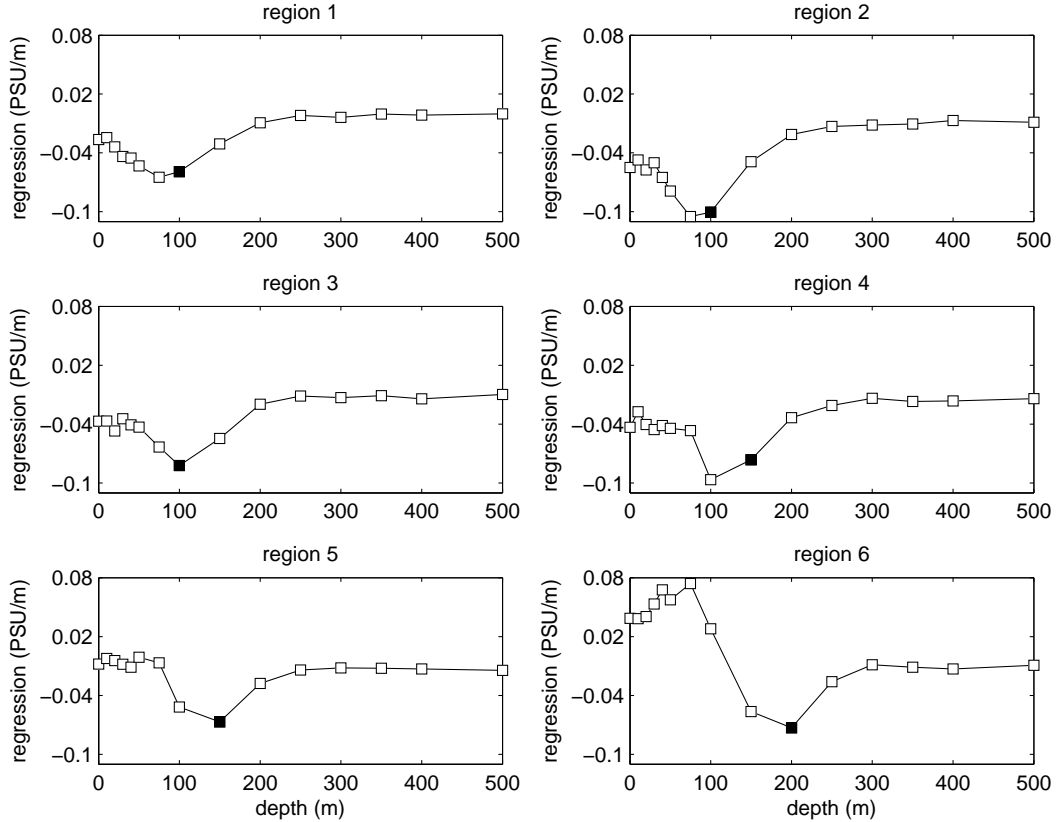


Figure 3.10: Regression coefficients between anomalies of salinity and anomalies of dynamic height. The solid square represents the maximum correlation in the first 500 meters. The regions are separated according to Fig. 2.1.

temperature in which interdecadal variability is a minor contributor.

To understand the salinity variability, particularly the interdecadal variability, we will use equation (3.38), estimating the anomalous evaporation E' for the CalCOFI region from (3.33) and wind and humidity data from the International Comprehensive Ocean Atmosphere Data Set (ICOADS, see <http://www.cdc.noaa.gov/>). The agreement between observed S' and S' predicted from (3.38) given η' the sea level at the coast and E' is modest (see Fig. 3.12). The correlation between region 1 CalCOFI salinity anomaly is $r=0.58$ with $r(90\% \text{ critical})=0.56$ using the method of Ebisuzaki (1997)[2]. When the predicted time series is correlated with the salinity at the coast $r=0.57$, and $r(95\% \text{ critical})=0.56$.

The two contributions to S' on the right hand side of (3.38) are shown in Fig. 3.13. The advection contribution proportional to η' is negligible and the anomalous evaporation

contribution, proportional to $\int_0^t E' dt$, is mainly interdecadal. The interdecadal variability is prominent in the evaporation term because the time integral acts like a low pass filter.

Given the above evidence for the dominant role of evaporation in interdecadal upper ocean salinity variability, it is useful to consider the contributions to E' . The linearized anomaly version of (3.33) is

$$E' = \rho_a c_E (q'_s - q'_a) |\mathbf{u}_a| + \rho_a c_E (q_s - q_a) |\mathbf{u}_a|. \quad (3.39)$$

Calculations show that the first term on the left hand side of (3.39) is better correlated with E' than the second and the first terms RMS value is 1.3 times the second (see Fig. 3.14). Thus it is the specific humidity anomaly, rather than the wind speed anomaly, that contributes most to the evaporation anomaly.

3.6 Concluding remarks

Several conclusions follow from the above analysis. First, especially for the large low frequency fluctuations near the halocline, salinity and temperature fluctuations seem to be mainly due to vertical and alongshore velocity anomalies acting on the mean vertical and alongshore salinity and temperature gradients. The vertical and alongshore velocity anomalies are associated with long, westward propagating waves in the CalCOFI region. Second, while temperature anomalies in the 100 m deep surface layer are little affected by surface fluxes of heat, much of the salinity variability near the surface is due to anomalous evaporation. This evaporative flux appears to give rise to interdecadal salinity fluctuations in the top 100 m of the CalCOFI region. The anomalous evaporation is mainly due to the specific humidity anomaly rather than the wind speed anomaly.

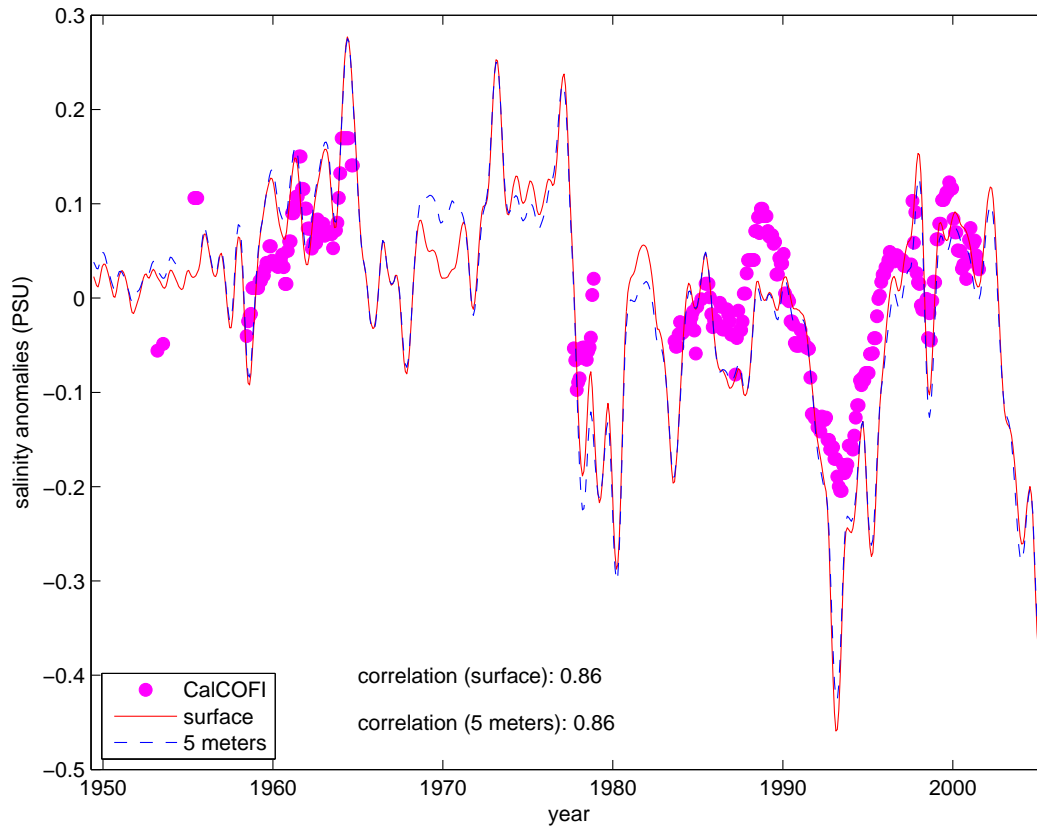


Figure 3.11: Interannual coastal La Jolla surface salinity anomaly (solid curve), 5 meter depth coastal La Jolla salinity anomaly (dashed curve) and the anomalous salinity averaged over region 1 in the upper 100 meters of the water column (dots). The correlation between each coastal time series and region 1 is 0.86 which is significantly different from zero (critical regression at 95%=0.59) according to Ebisuzaki (1997)[2]. The coastal surface and 5 m depth salinity time series were obtained from the Stephen Birch Aquarium-Museum at the Scripps Institute of Oceanography.

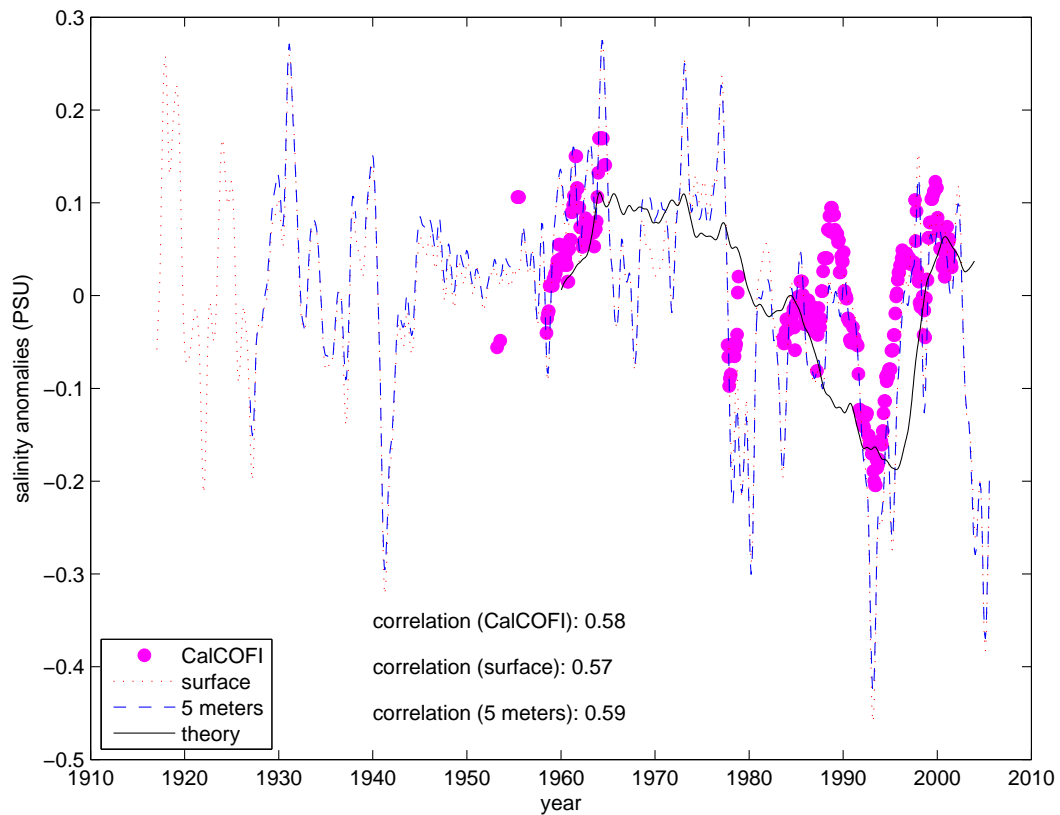


Figure 3.12: Observed region 1 CalCOFI salinity anomalies averaged over the upper 100 meters of the water column (large dots), coastal La Jolla surface (small dots), 5 m depth (dash-dot) and predicted anomalous salinity (solid line). The correlation coefficients are significantly different from zero at the 90% level for region 1 CalCOFI time series and 95% for La Jolla salinity at the surface and 5 meters deep according to Ebisuzaki (1997) [2].

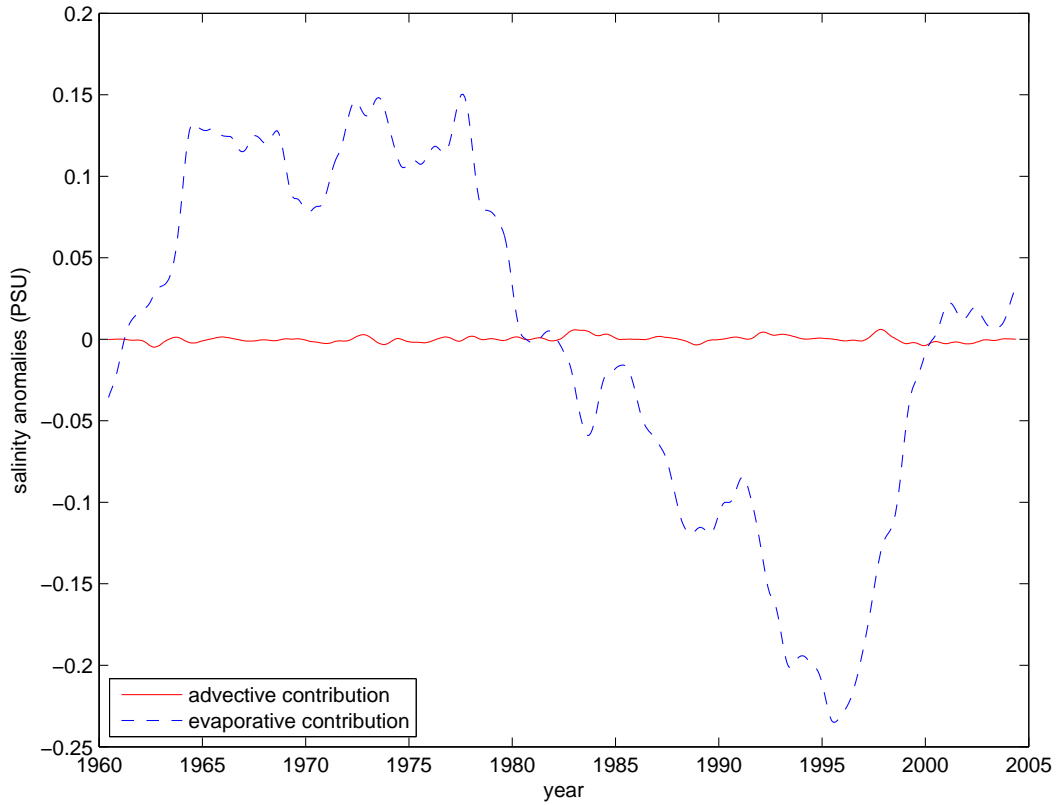


Figure 3.13: Advective (solid line) and evaporative (dashed line) contributions to anomalous salinity according to (3.38). In Eq. (3.38) the advective contribution is proportional to η' and the evaporative contribution is proportion to the time integral of E' .

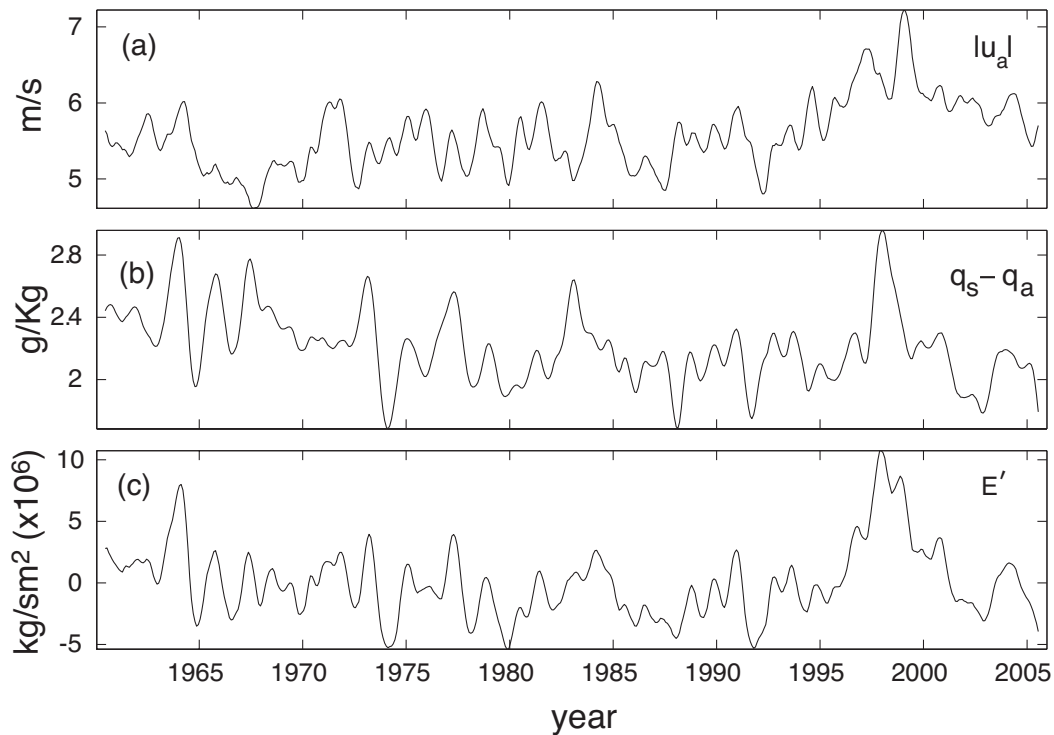


Figure 3.14: (a) Wind speed $|\mathbf{u}_a|$, (b) specific humidity different $q_s - q_a$ and (c) anomalous evaporation E' over the CalCOFI region using the International Comprehensive Ocean Atmosphere Data Set (ICOADS) (<http://icoads.noaa.gov/>).

CHAPTER 4

CONCLUSIONS

Low-frequency dynamics near the California coast seems to be dominated by a remote signal of equatorial origin. The interannual sea-level variability is strongly associated with El Niño/La Niña cycles. Although previous work has shown a poleward propagation for the western coast of the Americas, at the coast of California such propagation is not observed, with all coastal stations oscillating in phase and with very similar amplitudes for the interannual signal. However, it's not possible to say that this coastal propagation does not exist, since it would take less than a month for the interannual signal to cross the whole coast of California at the speeds observed by Enfield and Allen (1980)[3] and Chelton and Davis (1982)[4].

Offshore, the interannual dynamic height is strongly lag-correlated with the interannual sea-level at the coast, suggesting a Rossby wave behavior. The lags between dynamic height and the sea-level at the coast increase with the distance offshore and a linear regression gives a propagation speed about 4 cm/s. However, the large-scale theories available at the moment cannot explain this speed. The standard theory and more complete ones including zonal background flow and bottom topography estimate the westward propagation about 2 cm/s, half the velocity observed from hydrography.

Satellite altimeter measurements more complete spatially and temporally, but having a much shorter record, give similar results to the hydrography. The interannual sea surface altimeter height (SSH) lags the coastal sea-level, the lags increasing with increasing distance westward from the coast. The westward propagation speed estimated by linear regression between the lags and the offshore distance is close to 4cm/s, very similar to the speed found from hydrography.

Because of the westward propagation, interannual variations in alongshore geostrophic

surface current are proportional to the time derivative of sea level. These variations can, therefore, be easily estimated by the appropriately lagged derivative of coastal sea-level. Since the anomalous alongshore velocity is proportional to the time derivative of coastal sea level, the anomalous alongshore displacement is proportional to the anomalous sea level itself. Above normal coastal sea level results in anomalous northward particle displacement along the coast, transporting northward warmer water that is lower in nutrients. Conversely, lower than normal coastal sea level is associated with southward movement of colder water that is higher in nutrients. Anomalous sea level is also proportional to vertical displacements in the water column which causes temperature and nutrient anomalies of the same sign as the alongshore displacement. As a result, sea level anomalies are correlated positively with temperature anomalies. The nutrient data are not sufficiently plentiful to show that they are negatively correlated with the sea level anomalies. However, theory suggested that the logarithm of the zooplankton population should be correlated with the nutrients and hence sea level anomalies and calculations verified this. Consistent with the westward Rossby wave, the logarithm, of the zooplankton population averaged over the CalCOFI region is well correlated with the coastal sea level and lags it by about 2 months. By this result, monthly anomalous San Diego sea level can be used to monitor and predict interannual changes in the CalCOFI zooplankton population.

Salinity anomalies in the CalCOFI region are small. Beneath the upper 100 meters they are due to alongshore and vertical advection but, unlike temperature, the alongshore and vertical advection contributions are of opposite sign. The vertical advection dominates, however, a positive sea level anomaly resulting in downward displacement of fresh water and a consequent negative salinity anomaly. Conversely, a negative sea level anomaly results in an upward displacement of saltier water and a positive salinity anomaly.

In the 100 meter surface layer anomalous evaporation, rather than anomalous advection, determines the salinity anomaly. The surface salinity anomaly is a time integration of the anomalous evaporation and so is a low-pass filter of it. Consequently, the surface salinity is mainly interdecadal rather than interannual. The anomalous evaporation which drives this interdecadal salinity is mainly due to anomalous humidity difference between the air and the sea surface rather than the wind speed anomaly.

APPENDIX A

The effect of mean meridional flow on long Rossby waves

Here a simple model is considered to highlight the influence of mean meridional flow on long Rossby waves. Clarke and Li (2004)[15] analyzed a similar model but in their case the mean flow was strong enough that the dynamics could be taken to be quasi-steady. The model has two layers of fluid of constant density, the upper layer of depth h being much thinner than the lower layer. Under the assumption that the local wind forcing is negligible and that the flow is of large enough scale that the relative vorticity can be neglected, the upper layer flow is governed by the conservation of the large-scale potential vorticity:

$$\left(\frac{\partial}{\partial t} + \mathbf{u}\nabla \right) \frac{f}{g} = 0 \quad (\text{A.1})$$

In A.1 is the upper layer horizontal velocity, ∇ the horizontal gradient operator, t the time and f the Coriolis parameter.

To examine the effect of the mean flow on the interannual flow, write

$$\mathbf{u} = \bar{\mathbf{u}} + \mathbf{u}', \quad h = \bar{h} + h' \quad (\text{A.2})$$

where the overbar refers to the time mean and the prime to the interannual deviation. The linearized anomalous version of A.1 for a small interannual perturbation is

$$\frac{\partial q'}{\partial t} + \bar{\mathbf{u}}g\nabla q' + \mathbf{u}'g\nabla \bar{q} = 0 \quad (\text{A.3})$$

where

$$q = \frac{f}{\bar{h}} \quad (\text{A.4})$$

and

$$q' = -\frac{fh'}{\bar{h}^2} \quad (\text{A.5})$$

Equation A.3 can be considerably simplified using the large-scale low-frequency result that $\bar{\mathbf{u}}$ and \mathbf{u}' are quasi-geostrophic:

$$\mathbf{u}' \approx \frac{g_*}{f} (\mathbf{k} \times \nabla h') \quad (\text{A.6})$$

and

$$\bar{\mathbf{u}} \approx \frac{g_*}{f} (\mathbf{k} \times \nabla \bar{h}) \quad (\text{A.7})$$

where \mathbf{k} is the unit upward vertical vector. In A.6 and A.7 $g_* = \frac{\delta\rho}{\rho}g$ is the reduced gravity, g , $\delta\rho$ and ρ referring to the acceleration due to gravity, the density difference between the two ocean layers and the density of the upper layer. It follows from A.6 and A.7 that

$$\bar{\mathbf{u}}\nabla\bar{h} \approx 0 \quad \text{and} \quad \mathbf{u}'\nabla\bar{h} + \bar{\mathbf{u}}\nabla h' = 0 \quad (\text{A.8})$$

Hence (A3) simplifies to

$$-\frac{fh_t}{\bar{h}} - h'\frac{\beta\bar{v}}{\bar{h}} + \beta v' \approx 0 \quad (\text{A.9})$$

where β is the northward gradient of f and v is the northward velocity.

Using the geostrophic relationship A.6 for v' in A.10 gives

$$h'_x - \frac{h'}{a} - \frac{h'_t}{\gamma} \approx 0 \quad (\text{A.10})$$

where x is the distance eastward, γ is the long wave Rossby wave speed

$$\gamma = \frac{\beta g_* \bar{h}}{f^2} \quad (\text{A.11})$$

and the length scale

$$a = \frac{C C}{f \bar{v}} \quad (\text{A.12})$$

with C as the long internal gravity wave speed $(g_* \bar{h})^{1/2}$.

The solution of A.10 is of the form

$$h' = \Phi \left(t + \frac{x}{a} \right) e^{x/a} \quad (\text{A.13})$$

for some differentiable function Φ . Equation A.13 represents a long wave propagating westward at speed γ with amplitude modified by the factor $e^{x/a}$. For the California current $C \approx 2.5m/s$, $f \approx 8 \times 10^{-5}$, and $\bar{v} \approx 5cm/s$ which leads to $a \approx -1560km$. Since x is more negative with increasing distance seaward from the coast, A.10 predicts that h' should increase by about 50% over the measurement array (maximum zonal distance from the coast at $x = 0$ is approximately 700 km). This is in marked contrast with the amplitude decrease seen in Fig. 2.3.

REFERENCES

- [1] K. E. Trenberth. Signal versus noise in the Southern Oscillation. *Monthly Weather Review*, 112:326–332, 1984.
- [2] W. Ebisuzaki. A method to estimate the statistical significance of a correlation when the data are serially correlated. *Journal of Climate*, 10:2147–2153, 1997.
- [3] D. B. Enfield and J. S. Allen. On the structure and dynamics of monthly mean sea level anomalies along the Pacific coast of North and South America. *Journal Phys. Oceanogr.*, 10:557–578, 1980.
- [4] D. B. Chelton and R. E. Davis. Monthly mean sea-level variability along the west coast of North America. *Journal Phys. Oceanogr.*, 12:757–784, 1982.
- [5] D. B. Chelton, P. A. Bernal, and J. A. McGowan. Large-scale interannual physical and biological interaction in the California Current. *Journal of Marine Research*, 40(4):1095–1125, 1982.
- [6] W. S. Kessler. Observations of long Rossby waves in the Northern Tropical Pacific. *Journal Phys. Oceanogr.*, 95:5183–5217, 1990.
- [7] P. S. Schopf, D. L. Anderson, and R. Smith. Beta-dispersion of low-frequency Rossby wave. *Dyn. Atmospheres and Oceans*, 5:187–214, 1981.
- [8] M. A. Cane and D. W. Moore. A note on low-frequency equatorial basin modes. *Journal Phys. Oceanogr.*, 11:1578–1584, 1981.
- [9] A. J. Clarke. The reflection of equatorial waves from oceanic boundaries. *Journal Phys. Oceanogr.*, 13:1193–1207, 1983.
- [10] W. B. White and J. F. T. Saur. Sources of interannual baroclinic waves in the eastern subtropical North Pacific. *Journal Phys. Oceanogr.*, 13:531–544, 1983.
- [11] A. J. Miller, W. B. White, and D. R. Cayan. North Pacific thermocline variations on ENSO timescales. *Journal Phys. Oceanogr.*, 27:2023–2039, 1997.
- [12] P. D. Killworth, D. B. Chelton, and R. A. Szoeké. The speed of observed and theoretical long extratropical planetary waves. *Journal Phys. Oceanogr.*, 27:1946–1966, 1997.
- [13] W. K. Dewar. On too fast baroclinic planetary waves in the general circulation. *Journal Phys. Oceanogr.*, 28:1739–1758, 1998.

- [14] W. K. Dewar and M. Y. Morris. On the propagation of baroclinic waves in the general circulation. *Journal Phys. Oceanogr.*, 30:2637–2649, 2000.
- [15] A. J. Clarke and Jianke Lee. El Niño La Niña shelf edge flow and Australian Western Rock Lobster. *Geophys. Res. Letters*, 31:LXX–LXXX, 2004.
- [16] P. D. Killworth and J. R. Blundell. Long extratropical planetary wave propagation in the presence of slowly varying mean flow and bottom topography. *Journal Phys. Oceanogr.*, 33:784–801, 2002.
- [17] N. Schneider, E. DiLorenzo, and P. P. Niiler. Salinity variations in the Southern California current. *Journal Phys. Oceanogr.*, 35:1421–1436, 2005.
- [18] C. S. Roesler and D. B. Chelton. Zooplankton variability in the California Current, 1951-1982. *Calif. Coop. Oceanic Fish. Invest. Repts.*, 28:59–96, 1987.
- [19] L. L. Fu and B. Qiu. Low-frequency variability of the North Pacific Ocean: The role of boundary- and wind-driven baroclinic Rossby waves. *Journal Geophys. Res.*, 107:3220, doi:10.1029/2001JC001131, 2002.
- [20] A. E. Gill. *Atmosphere-Ocean Dynamics*. Academic Press, Boston-MA, 1982.
- [21] S. Levitus. *Climatological Atlas of the World Ocean.*, volume 13. 1982.
- [22] P. D. Killworth and J. R. Blundell. The effect of bottom topography on the speed of long extratropical planetary waves. *Journal Phys. Oceanogr.*, 29:2689–2710, 1999.
- [23] R. Tailleux and J. C. McWilliams. The effect of bottom pressure decoupling on the speed of extratropical, baroclinic Rossby waves. *Journal Phys. Oceanogr.*, 31:1461–1476, 2001.
- [24] J. Li and A. J. Clarke. Coastline direction, interannual flow and the strong El Nio currents along Australias nearly zonal southern coast. *Journal Phys. Oceanogr.*, 34(11):2373–2381, 2004.
- [25] S. J. Bograd, T. K. Chereskin, and D. Roemmich. Transport of mass, heat, salt, and nutrients in the southern California Current system: Annual cycle and interannual variability. *Journal Geophys. Res.*, 106(C5):9255–9275, 2001.
- [26] A. E. Gill and A. J. Clarke. Wind-induced upwelling, coastal currents and sea-level changes. *Deep-sea Reasearch*, 21:325–345, 1974.
- [27] A. J. Clarke and C. Shi. Critical frequencies at ocean boundaries. *Journal Geophys. Res.*, 96:10731–10738, 1991.

BIOGRAPHICAL SKETCH

Marcelo Dottori

Marcelo Dottori was born in São Bernardo do Campo (SP, Brazil) on August 25, 1971. He lived his whole life in São Paulo, Brazil, until he moved to Tallahassee, FL, in January 2002. In December 1998 he graduated with a Bachelors degree in physics at Universidade de São Paulo, São Paulo, Brazil. The year after he started his Masters program at the same university. In November 2001 he obtained the degree of Masters of Physical Oceanography, working with Dr. Belmiro Mendes de Castro Filho. In the spring of 2002 he began in the doctoral program at the Department of Oceanography at Florida State University. Since then, he has been working with Dr. Allan J. Clarke in the field of coastal interannual dynamics.

Marcelo's research interests include coastal dynamics, the influence of physical processes on biology, numerical models and satellite data analyses.